Off the Planckian Locus: Using 2D Chromaticity to Improve In-Camera Color

SaiKiran Tedla¹ Joshua E. Little¹ Hakki Can Karaimer² Michael S. Brown¹ York University ²AI Center-Toronto, Samsung Electronics

{tedlasai,jelittle,mbrown}@yorku.ca {hakki.k}@samsung.com

Abstract

Traditional in-camera colorimetric mapping relies on correlated color temperature (CCT)-based interpolation between pre-calibrated transforms optimized for Planckian illuminants such as CIE A and D65. However, modern lighting technologies such as LEDs can deviate substantially from the Planckian locus, exposing the limitations of relying on conventional one-dimensional CCT for illumination characterization. This paper demonstrates that transitioning from 1D CCT (on the Planckian locus) to a 2D chromaticity space (off the Planckian locus) improves colorimetric accuracy across various mapping approaches. In addition, we replace conventional CCT interpolation with a lightweight multi-layer perceptron (MLP) that leverages 2D chromaticity features for robust colorimetric mapping under non-Planckian illuminants. A lightbox-based calibration procedure incorporating representative LED sources is used to train our MLP. Validated across diverse LED lighting, our method reduces angular reproduction error by 22% on average in LED-lit scenes, maintains backward compatibility with traditional illuminants, accommodates multi-illuminant scenes, and supports real-time in-camera deployment with negligible additional computational cost. Project page: https://cst-mlp.github.io

1. Introduction

Digital cameras perform a wide range of in-camera processing routines to convert sensor-specific RGB responses into the final output image [16]. A critical component of the in-camera processing pipeline is the colorimetric mapping stage, which performs illumination correction followed by a color space transformation (CST) to map sensor values to a standard color space such as CIE XYZ [15]. The accuracy of this colorimetric mapping directly impacts color reproduction quality across different lighting conditions.

The current in-camera colorimetric mapping method was developed when early digital cameras primarily captured images illuminated by conventional light sources (e.g., incandescent, fluorescent, and natural/outdoor light). The per-

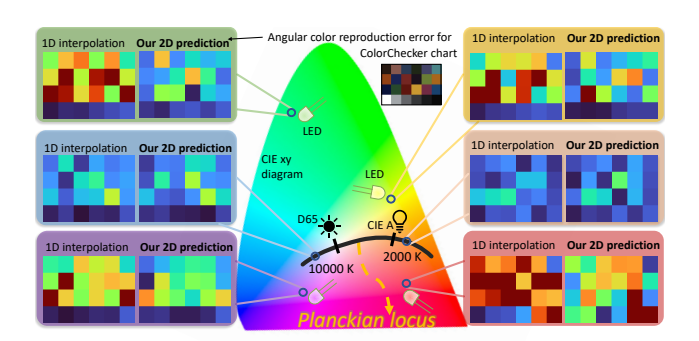


Figure 1. 1D Planckian interpolation vs. our 2D chromaticity-based prediction. Traditional 1D methods perform adequately for light sources whose CCTs lie close to the Planckian locus but are notably less accurate for light sources (namely, LEDs) that lie off the Planckian locus. Our approach leverages 2D chromaticity coordinates for more robust color reproduction across all illuminant types. Heat maps show angular reproduction error, from 0° (dark blue) to 15° (dark red), demonstrating comparable performance along the Planckian curve but substantial improvements in LED-dominated regions where existing methods break down.

ceived colors of these early light sources' spectra are conveniently correlated with blackbody radiators—idealized physical bodies whose spectral distributions depend solely on temperature according to Planck's law [53]. In the CIE xy chromaticity space [15], these blackbody sources form the Planckian locus, as shown in Figure 1. Correlated color temperature (CCT) provides a simple 1D representation for characterizing such conventional light sources. The standard procedure for CST computation involves one-dimensional CCT-based interpolation of pre-calibrated matrices along the Planckian locus. Typically, two pre-calibrated illuminants are used (1) daylight 6500 K temperature and (2) incandescent light (CIE A).

However, the proliferation of LED technology has fundamentally disrupted this framework. Modern artificial illuminants exhibit chromaticity coordinates that deviate significantly from the Planckian locus, resulting in suboptimal color reproduction when using CCT-based interpolation (Figure 1). This mismatch highlights the growing disparity between current camera color-processing assumptions and

the spectral characteristics of modern illumination.

This paper proposes shifting from a one-dimensional CCT space to a 2D chromaticity space for CST estimation. Our approach recognizes that modern illuminants require characterization beyond simple CCT, incorporating camera-specific chromaticity coordinates as input features. Moreover, we employ a lightweight multi-layered perceptron network to learn optimal interpolation. By training on an expanded dataset including representative LED illuminants alongside traditional sources, our CST-MLP achieves superior colorimetric mapping that adapts to contemporary lighting spectral diversity while maintaining backward compatibility.

Our key contributions are as follows: (1) CST-MLP, a lightweight MLP that predicts CSTs in 2D chromaticity space, replacing traditional CCT-based interpolation with learned transforms capable of handling non-Planckian illuminants; (2) adaptation of traditional and baseline methods to operate in the chromaticity domain; (3) extensive validation demonstrating an average 22% improvement in color reproduction accuracy across two smartphones and two DSLRs; (4) a spatially varying extension for multi-illuminant scenarios; and (5) a carefully collected laboratory and in-the-wild dataset captured under non-Planckian illuminants for evaluating our method. This work represents a step toward modernizing in-camera color processing in line with the widespread adoption of LED lighting.

2. Motivation and Related Work

Motivation. The colorimetric mapping stage of the digital camera pipeline (top/middle of Figure 2 consists of two main steps: white balance (WB) via a diagonal correction and color balance (CB) via a CST. In the camera pipeline, WB is typically modeled in the 2D raw chromaticity space [26]. Other software, such as Lightroom [2], allows 2D WB control via temperature and tint [43] sliders. While estimated WB values are represented in 2D chromaticity space, the color-balancing stage of the camera pipeline projects 2D chromaticities onto a 1D CCT and utilizes a CCT-based interpolation [1] to derive the CST (see Supplementary Section S5 for details on this procedure).

CCT-based interpolation assumes that conventional light sources lie close to the Planckian locus, however, LEDs and tunable lighting violate the core assumption, as their chromaticity coordinates often deviate significantly from the Planckian locus [5, 42]. This divergence arises from inherent LED properties, including discontinuous spectra [28] and narrow-band primaries [47].

When illumination chromaticity coordinates fall far from the Planckian locus, CCT calculations become ill-defined [43], and subsequent CCT-based interpolation leads to errors exceeding just-noticeable color differences [7]. Karaimer and Brown [27] introduced an additional calibra-

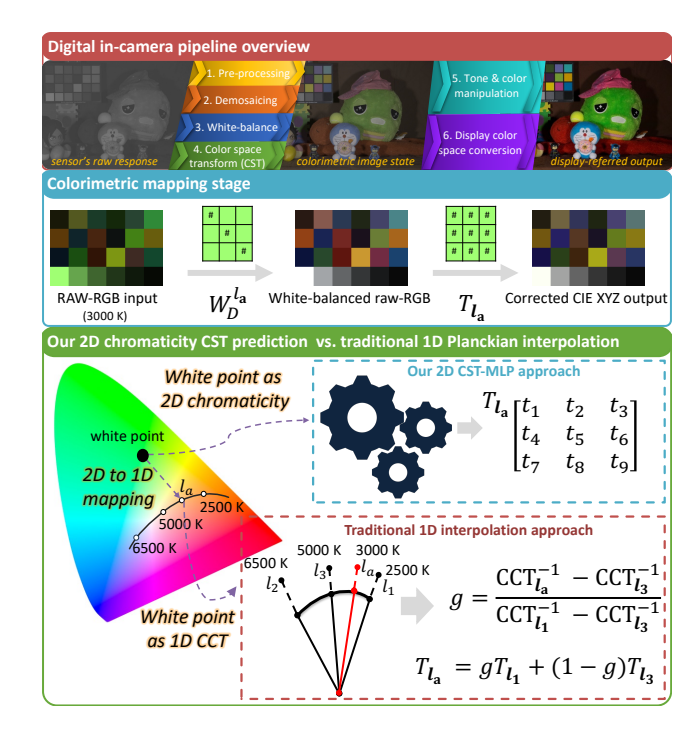


Figure 2. Top: Camera pipeline overview. Early stages convert raw sensor responses to colorimetric values, while later stages transform colors to a photo-finished display-referred space [26]. This paper aims to achieve maximum accuracy in the colorimetric stage. Middle: Colorimetric mapping stage. When an image is captured under arbitrary illumination, the estimated illumination is used to remove color cast via a diagonal white-balance 3×3 matrix (i.e., $W_D^{l_a}$), then mapped to CIE XYZ with an illuminationspecific 3×3 CST matrix (i.e., T_{l_a}). Bottom: 2D chromaticity CST prediction vs. 1D CCT interpolation. CST interpolation approaches (e.g., $T_{l_a} = gT_{2500K} + (1 - g)T_{6500K}$) assume CST parameters can be derived from a CCT-based interpolation, given calibrated illuminants along the Planckian Locus. CCT-based interpolation works poorly for non-Planckian illuminants. We propose a 2D CST-MLP that takes chromaticity coordinates as input and directly predicts the full 3×3 CST matrix.

tion point along the Planckian locus to improve interpolation, an approach later integrated into the Adobe DNG specification [1]. However, because it still relies on CCT-based interpolation, this method cannot represent light sources that fall off the Planckian locus. Other research has explored improved illumination estimation [9, 23, 30, 54] and post-processing strategies [13, 19, 27, 48], yet these approaches do not address the fundamental limitation of CCT-based interpolation in the colorimetric mapping stage. To overcome this, we propose predicting the CST directly in the 2D chromaticity space using a CST-MLP, as illustrated in Figure 2 (bottom).

In the following, we present a short review of relevant areas for in-camera color reproduction.

Color constancy. Early color-correction stages in camera

ISP are motivated by the human visual system's color constancy ability to perceive object colors similarly under different illuminations. Computational color constancy generates sensor responses that are invariant to scene illumination in two steps: estimating scene illumination in raw sensor space, then removing the color cast.

White balance. Most color constancy works focus on illu-

mination estimation using classical statistics, gamut-based methods [6, 14, 18, 20, 21, 51], and deep-learning approaches [4, 35, 37, 48]. After illuminant estimation, correction typically applies a diagonal 3×3 matrix to the raw-RGB image. Simple WB correction only ensures proper correction of neutral colors (R = G = B after correction). Color balance. Additional correction is required for nonneutral colors. Thus, diagonal correction provides white balance (WB), while full correction is color balance (CB). Diagonal correction suffices for particular illuminations (e.g., broadband) to achieve full CB, but many illuminations require full color balancing [11]. Camera ISPs apply an illumination-specific CST [27] after WB to correct nonneutral colors. Adobe DNG implements this by mapping illuminants to CCT, then interpolating between calibrated 3×3 CST matrices that map to CIE XYZ. Initially, DNG supported two CST matrices at high (~6500 K) and low $(\sim 2500 \text{ K})$ CCT. Karaimer and Brown [27] showed that an additional calibration point (~4300 K) improves reproduc-

tion, resulting in DNG now supporting three CSTs. Other

higher-dimensional mappings, such as polynomial [12] and

root-polynomial [19], could be used in place of the 3×3

transformation; however, these mappings are prone to over-

fitting [19] and are non-invertible.

Direct mapping. Recent methods such as CCCNN [38] and EXPINV [33] learn an illuminant-dependent colorimetric mapping by training MLPs that take raw pixel values and illuminant CCT as input to predict CIE XYZ values directly. However, these networks require expensive perpixel evaluation at test time and rely on access to camera spectral sensitivities during training. Their pixel-wise formulation introduces spatial inconsistencies and color casts, as we demonstrate in Section 4.2. Finally, their dependence on 1D CCT illumination coordinates limits these networks' ability to model non-Planckian illuminants. In contrast, our proposed CST-MLP predicts a global CST in a single forward pass, enforces spatial consistency, requires no spectral sensitivity data, and generalizes better across diverse light sources by operating in 2D chromaticity space.

3. Method

We aim to learn a mapping from illuminant chromaticity to a CST using a two-stage method, visualized in Figure 3, involving calibration data capture within a lightbox (Section 3.1) and training a lightweight CST-MLP (Section 3.2).

3.1. Data Capture

Traditional CST calibration methods calibrate CSTs by capturing color charts under standard illuminants such as CIE A or D65. However, we require our method to handle non-Planckian illuminants that a CCT cannot adequately describe. The first step in our process is to capture calibration data across diverse illuminants so our model learns the correct CST under diverse lighting conditions.

We use a modified GTI lightbox [22] to capture a ColorChecker [8] target under a wide range of lighting conditions. This modified lightbox replaces the original light sources with Telelumen multispectral LED lighting [50], which consists of seven narrow-band LEDs that can be adjusted to match a target spectral power distribution (SPD). Using the Telelumen lightbox, we capture the color chart under many SPDs, resulting in a large calibration dataset.

We capture each color chart under 790 different illuminant SPDs sourced from two methods. First, we utilize 390 illuminants from Punnappurath et al. [45] that estimate various light sources, including sunlight, fluorescent, incandescent, and LED. We use the original splits of 195 training, 78 validation, and 117 test illuminants. Then, we introduce a set of 400 illuminants generated by linearly combining the Telelumen LED SPDs with weights randomly sampled from a Dirichlet distribution (see Supplementary Section S2 for details). Using this distribution results in an even spread of illuminants across the chromaticity space and allows us to sample more illuminants farther from the Planckian Locus. We randomly split the dataset into 200 train, 80 validation, and 120 test illuminants. We combine both datasets for our calibration, resulting in 395 train, 158 validation, and 237 test illuminants.

3.2. Model

We propose a model, CST-MLP, that maps a white-point chromaticity w_{xy} to a CST T. Following Karaimer and Brown [27], we use the setting of mapping white-balanced raw images into the XYZ canonical space, and assume the raw image I_{raw} and ground-truth white point chromaticity w = [r/g, b/g] are known. Following previous work [27], we use the ground-truth white point from the color chart white patch and compute the white-balanced raw image I_{wb} , by applying a diagonal correction [4]. For our model, we convert the raw-space chromaticity w to its xy-space counterpart w_{xy} using the DNG [1] optimization procedure described in Supplementary Section S5.

CST-MLP is a small network with one hidden layer of 32 units that predicts the eight free entries of a 3×3 CST matrix. Since the CST is defined only up to scale due to the angular-error loss, we fix the central element of the matrix to 1 to remove this ambiguity. The eight predicted values are then reshaped into the CST matrix. CST-MLP is constrained to predict linear color transformations to maintain

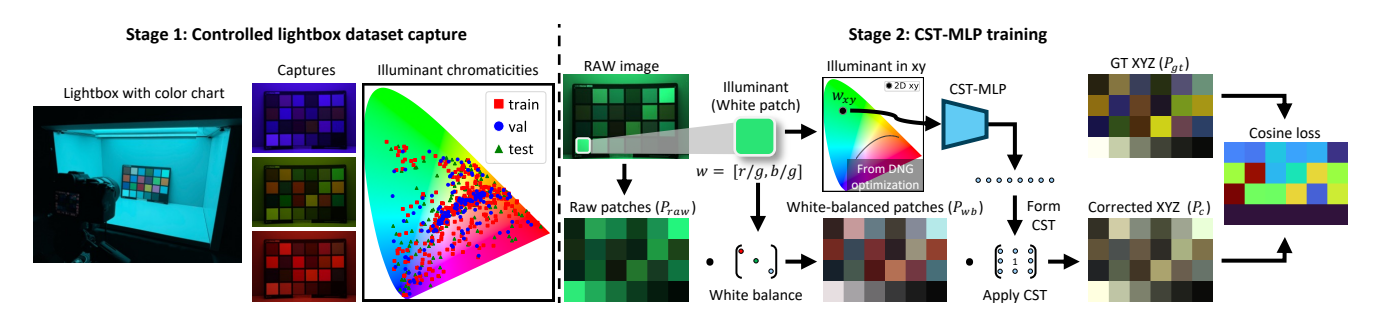


Figure 3. Our 2D chromaticity CST prediction framework. (Stage 1) Controlled lightbox dataset capture: A ColorChecker [8] target is captured under diverse illumination, including traditional Planckian sources and modern LED illuminants with varying chromaticity coordinates, ensuring comprehensive coverage of on-locus and off-locus illuminants. (Stage 2) CST-MLP training: Our lightweight MLP takes 2D chromaticity coordinates as input and predicts the color space transform directly, bypassing CCT-based interpolation. To train CST-MLP, we begin with raw color patches $P_{\rm raw}$ and apply white balancing using the estimated illuminant w (derived from the white patch), resulting in white-balanced patches $P_{\rm wb}$. We then convert the illuminant w into chromaticity coordinates w_{xy} via the DNG optimization procedure (see Supplementary Section S5). The chromaticity w_{xy} serves as input to our CST-MLP, which predicts the CST applied to $P_{\rm wb}$. Finally, we train with a cosine loss between the corrected patches P_c and the ground-truth patches $P_{\rm gt}$ in XYZ space.

compatibility with the DNG pipeline. Polynomial and root-polynomial variants are discussed in Supplementary Section S1.3.

To train our method, we extract the mean color of the 24 patches in the raw image $P_{raw} \in \mathbb{R}^{24 \times 3}$ by averaging across an 11×11 pixel region per patch. We then apply a diagonal white balance to each patch using the white patch w, resulting in white-balanced patches $P_{\rm wb}$. For a given illumination, the model aims to predict a 3×3 CST that when applied to P_{wb} minimizes the angular error between the corrected XYZ patches $P_c \in \mathbb{R}^{24 \times 3}$ and the ground-truth XYZ $P_{gt} \in \mathbb{R}^{24 \times 3}$.

We utilize our calibration dataset to train the model and use the ground-truth XYZ values provided by X-Rite [8] for the color chart. Following Karaimer and Brown [27], we aim to minimize the angular error of the corrected XYZ colors and the ground-truth XYZ colors. We found direct angular error loss was unstable during optimization; thus, we follow other works [46, 52] and use a cosine loss, which still minimizes angular errors [52]. We define the loss function as the average cosine loss over all color patches:

$$L(P_c, P_{gt}) = \frac{1}{n} \sum_{i=1}^{N} \left(1 - \cos\left(\hat{P}_c^i, \hat{P}_{gt}^i\right) \right), \quad (1)$$

where $\hat{P_c^i}$ and $\hat{P_{gt}^i}$ are the normalized colors at index i.

4. Evaluation

First, we evaluate 1D CCT vs. 2D chromaticity-based approaches using the light box dataset described in Section 3.1. Next, we test our light-box calibration across a set of in-the-wild scenes. Finally, we compare our method on single-illuminant scenes from the LSMI [29] dataset and further extend the evaluation to multi-illuminant settings.

4.1. Evaluation Details

Baselines. For comparison, we implement a wide variety of state-of-the-art baselines. First, to contextualize the upper bound of CST prediction, we compute the Oracle, the best-fit 3×3 matrix that minimizes the angular error given the full color chart. Then, we compare with the standard 2-CST interpolation described by the DNG [1], which uses matrices recalibrated by capturing the color chart under Standard Illuminant A (2850 K) and D65 (6500 K) lighting within the lightbox. We also compare to the 3-CST [27] interpolation with an additional calibrated CST at 4250 K. Next, we implement a nearest neighbors (NN) [44] baseline that maps each training white point with its best-fit 3×3 CST (minimizing angular error on the color chart). At test time, given a white-point coordinate, we retrieve the nearest illuminant by L2 distance and apply its corresponding matrix. Finally, we compare direct MLP methods, CC-CNN [38] and EXPINV [33], that perform per-pixel correction given an input color and white point.

1D CCT vs 2D Chromaticity. To demonstrate the importance of using 2D chromaticity coordinates, we also compare our CST-MLP with a 1D CCT-based variant. Additionally, we adapt the 1D CCT-based baseline methods (NN, EXPINV, and CCCNN) into 2D chromaticity-based versions to show the benefits of our approach.

Training details. We use the dataset splits in Section 3.1 to train and evaluate all methods outside of CCCNN [38] and EXPINV [33]. As described in the original papers, CCCNN [38] and EXPINV [33] require a larger simulated dataset, as these networks aim to learn a per-pixel mapping. For simulation, we measure each camera's spectral sensitivities using CamspecV2 [25], illumination SPDs from

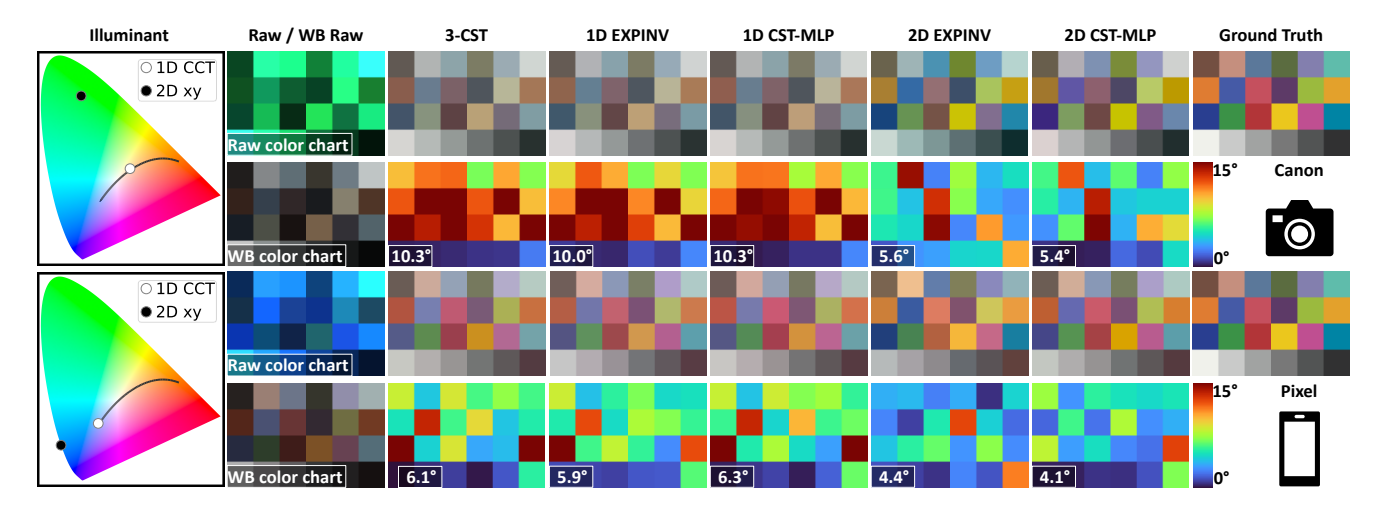


Figure 4. Colorimetric mapping results on laboratory dataset. Results for two non-Planckian LED sources: green LED (top half) and blue LED (bottom half) illuminants, captured using Canon and Pixel cameras. Each half starts with the illuminant's CCT and xy chromaticity and contains two rows: the top row shows the raw-RGB color chart and display-referred renderings; the bottom row shows the white-balanced color chart and error maps. Methods: 2-CST [27], 1D EXPINV [33], 1D CST-MLP, 2D EXPINV [33], 2D CST-MLP, and ground truth. Key findings: (1) Traditional 1D methods exhibit substantial errors for off-locus illuminants. (2) 2D chromaticity representation improves existing methods (compare 1D vs. 2D for EXPINV and CST-MLP).

our lightbox capture setup (see Section 3.1), and 1269 reflectance SPDs from the Munsell Book of Color [41]. We then synthesize data using the image formation model described in CCCNN [38] and EXPINV [33].

All MLP methods are trained for 100,000 iterations using the Adam [32] optimizer with a learning rate of 0.001. Our CST-MLP is trained using the cosine loss described in Section 3.2, while CCCNN [38] and EXPINV [33] are trained with the recommended ΔE loss.

Noise augmentation. When queried with out-of-domain chromaticities not seen in our training set, our 2D CST-MLP can sometimes fail to generalize. We fix this issue by adding Gaussian noise to input chromaticity coordinates at training time [34], allowing models to observe chromaticities that may be out of distribution. For CST-MLP, we add noise with standard deviation $\sigma_0 = 0.05$ to the normalized input coordinates for all training iterations. We show the positive effects of this augmentation in our ablation study (Table 2). Finally, we exclude this augmentation for direct-prediction MLP baselines (EXPINV [33], CCCNN [38]) as it can degrade their performance (see Supplementary Section S1.4).

Metrics. For evaluation, we utilize angular error following previous work [27]. We also compare ΔE_{2000} after applying a uniform scaling to all colors to match the Y channel of the third gray patch (bottom row of color chart). Finally, we report model parameter sizes (in KB) and inference costs (in MACs) when applied to a 1080×720 image.

4.2. Lightbox Dataset Results

We compare all methods quantitatively on our dataset in Table 1 and qualitatively in Figure 4 (additional visualizations in Supplementary Section S2). We find that *all methods benefit from using a 2D chromaticity coordinate* instead of a 1D CCT, which confirms our motivation for this work. Additionally, our 2D CST-MLP surpasses traditional interpolation and nearest-neighbor methods, providing a strong solution that integrates seamlessly into the existing DNG [1] pipeline, which relies on linear transformations.

Comparing CST-MLP with per-pixel MLPs. We find our 2D CST-MLP outperforms 1D MLP-based direct prediction baselines, CCCNN [38] and EXPINV [33]. Additionally, highlighting the strength of utilizing 2D chromaticity input, our 2D chromaticity-based variants of CC-CNN [38] and EXPINV [33] achieve lower ΔE_{2000} in many cases and surpass CST-MLP under challenging illumination conditions (higher percentiles). This performance gain arises because per-pixel MLPs can model more complex mappings, whereas our method is limited to predicting a linear transformation. However, per-pixel methods remain unsuitable for two reasons. First, CST-MLP has a footprint of 1.5 KB and 0.01 MMACs, compared to 69KB and 13 MMACs for per-pixel methods. CST-MLP is efficient because it predicts a single global transform. In Figure 5, we show that the computational cost of a per-pixel MLP far exceeds our CST-MLP at various input resolutions. Second, as shown in Figure 6, applying per-pixel MLP methods to fullsize images can produce color casts, likely because each

				Angular Error (°)																		
		C:	MACs			Sony	7				Cano	n				Pixe	I			Samsu	ng	
Method	Dim	(KB)	(M)	Mear	25%	50%	75%	90%	Mean	25%	50%	75%	90%	Mean	25%	50%	75%	90%	Mean	25% 50%	75%	90%
Oracle	1D	0.00	0.01	1.71	0.54	1.15	2.14	3.68	2.06	0.64	1.31	2.63	4.65	2.79	0.95	2.00	3.49	5.94	2.58	0.84 1.83	3.25	5.47
2-CST	1D	0.07	0.01	3.31	0.80	1.98	4.33	7.91	3.86	0.96	2.31	5.38	9.59	4.56	1.48	3.25	6.03	9.94	4.51	1.53 3.19	5.93	9.95
3-CST	1D	0.11	0.01	3.31	0.80	2.01	4.31	7.91	3.86	0.94	2.32	5.39	9.68	4.53	1.48	3.22	5.97	9.95	4.51	1.51 3.18	5.92	9.94
NN	1D	15.43	0.01	3.93	0.94	2.33	5.21	9.57	4.68	1.06	2.75	6.43	11.57	5.31	1.54	3.64	7.32	11.84	5.46	1.86 3.54	7.21	12.36
CCCNN	1D	68.51	13.39	3.13	0.99	2.02	4.07	7.21	3.58	1.13	2.40	4.71	8.14	4.41	1.53	3.10	5.81	9.64	4.63	1.53 3.34	6.25	10.05
EXPINV	1D	68.53	13.39	3.14	0.90	1.92	4.06	7.57	3.62	0.96	2.29	4.84	8.59	4.29	1.35	2.82	5.74	9.65	4.69	1.45 3.43	6.35	10.25
CST-MLP	1D	1.41	0.01	3.00	0.70	1.63	3.76	7.54	3.42	0.67	1.85	4.50	8.88	4.03	1.05	2.48	5.31	9.74	4.00	1.10 2.52	5.19	9.54
NN	2D	16.97	0.01	3.14	0.82	1.79	3.87	7.47	3.54	0.90	2.04	4.61	8.50	4.25	1.39	2.87	5.22	9.57	4.15	1.33 2.72	5.34	9.48
CCCNN	2D	69.01	13.48	2.89	0.97	1.99	3.83	6.43	3.00	1.13	2.20	3.91	6.19	4.00	1.50	2.93	5.20	8.76	4.17	1.78 3.32	5.51	8.52
EXPINV	2D	69.03	13.48	2.66	0.87	1.78	3.45	5.97	3.11	0.94	2.26	4.16	6.89	3.84	1.32	2.71	5.02	8.41	4.14	1.49 3.05	5.44	8.86
CST-MLP	2D	1.54	0.01	2.58	0.66	1.52	3.36	6.22	2.85	0.68	1.69	3.70	6.78	3.57	1.03	2.30	4.63	8.34	3.61	1.05 2.34	4.62	8.34
													ΔE	2000								
Oracle	1D	0.00	0.01	5.37	2.91	4.70	7.27	9.49	5.83	3.22	5.20	7.85	10.17	7.07	4.55	6.41	8.62	12.14	6.51	4.09 5.94	8.20	11.06
2-CST	1D	0.07	0.01	7.21	3.78	6.06	9.02	13.18	8.15	4.41	6.63	10.23	15.08	9.18	5.68	7.91	11.29	15.74	8.61	5.28 7.64	10.66	14.76
3-CST	1D	0.11	0.01	7.20	3.77	6.02	9.02	13.19	8.13	4.40	6.65	10.17	15.10	9.16	5.68	7.93	11.28	15.65	8.62	5.28 7.65	10.67	14.76
NN	1D	15.43	0.01	8.04	4.05	6.64	10.22	15.00	9.21	4.57	7.20	11.62	17.90	9.62	5.60	8.21	11.97	17.20	9.48	5.34 8.12	11.54	16.90
CCCNN	1D	68.51	13.39	7.03	3.54	6.12	9.81	12.55	7.72	4.11	6.74	10.49	13.85	8.30	4.92	7.27	10.65	14.15	8.27	4.53 7.74	10.63	14.05
EXPINV	1D	68.53	13.39	6.94	3.53	5.97	9.57	12.29	7.64	3.76	6.67	10.38	14.01	8.18	4.87	7.26	10.39	13.96	8.22	4.83 7.42	10.24	14.02
CST-MLP	1D	1.41	0.01	6.93	3.55	5.99	8.97	12.60	7.70	3.95	6.53	9.71	14.55	8.35	4.90	7.51	10.81	14.66	8.06	4.46 7.39	10.22	14.10
NN	2D	16.97	0.01	7.17	3.60	5.96	9.03	12.92	7.79	3.94	6.37	9.81	14.30	8.75	5.27	7.42	10.69	15.21	8.37	4.80 7.16	10.14	14.71
CCCNN	2D	69.01	13.48	6.63	3.69	5.62	9.17	11.40	6.78	3.58	6.07	9.27	11.61	8.07	4.88	7.42	10.33	12.91	7.76	4.86 7.66	9.47	11.96
EXPINV	2D	69.03	13.48	6.48	3.45	5.84	8.98	11.03	7.07	3.98	6.52	9.39	11.93	7.77	4.74	7.10	10.02	12.63	7.68	4.37 7.51	9.72	12.20
CST-MLP	2D	1.54	0.01	6.60	3.50	5.95	8.60	11.49	7.15	3.80	6.31	9.17	12.85	7.91	4.66	7.25	10.28	13.27	7.70	4.26 7.28	9.88	13.23

Table 1. Quantitative evaluation on lightbox dataset. We compare angular error and ΔE_{2000} of traditional 2-CST/3-CST interpolation [1, 27], NN [44], CCCNN [38], EXPINV [33], and our CST-MLP. For NN, CCCNN, EXPINV, and CST-MLP, we evaluate both 1D CCT-based implementations and our proposed 2D chromaticity-based adaptations (highlighted in blue).

pixel is transformed independently, leading to spatial inconsistencies. In contrast, CST-MLP applies a single transformation across the image, ensuring spatial consistency.

In-the-wild results. After calibrating the CST prediction methods with lightbox images, we evaluate on a smaller set of 64 in-the-wild photos captured with both smartphones (Pixel and Samsung). As shown in Figure 6, methods that rely on 2D chromaticity deliver qualitatively superior results, enabling more accurate color correction under challenging LED illumination across diverse regions containing skin tones, posters, and craft materials. We also observe that EXPINV [33], a per-pixel prediction method, exhibits color casts when applied to full-size images. Additional comparisons are provided in Supplementary Section S2.

Ablation. In Table 2, we ablate our choice of using a 2D xy chromaticity coordinate against modeling the illuminant in 1D CCT space or in 2D raw space. Additionally, we find that our noise augmentation strategy is crucial for our method to generalize to out-of-domain illuminant chromaticities. We further ablate CST-MLP with varying layer and node counts in Supplementary Section S1.4.

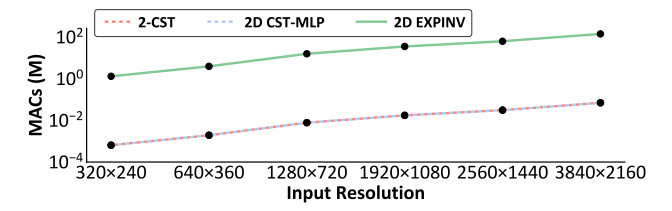


Figure 5. **Computational cost comparison.** We plot the MACs (log scale) at different resolutions for 2-CST [1] interpolation, EX-PINV [33], and 2D CST-MLP [33]. Our CST-MLP has nearly the same computational cost as traditional methods, since the CST is computed once and applied to the entire image. In contrast, approaches such as EXPINV must evaluate the MLP at every pixel.

Input	Noise	Lighth	ox	In-the-v	wild
coord.	Aug.	Ang. (°)	ΔE	Ang. (°)	ΔE
1D (CCT)	Х	4.03	8.35	4.86	8.48
2D (raw)	×	3.58	7.99	5.39	9.64
2D (raw)	✓	3.70	7.91	4.92	8.79
2D(xy)	×	3.53	7.92	5.04	9.12
2D(xy)	✓	3.57	7.91	4.47	8.29

Table 2. **Ablation of CST-MLP.** We evaluate CST-MLP on Pixel camera data from both lightbox and in-the-wild scenes, testing 1D and 2D input coordinates with and without noise augmentation.

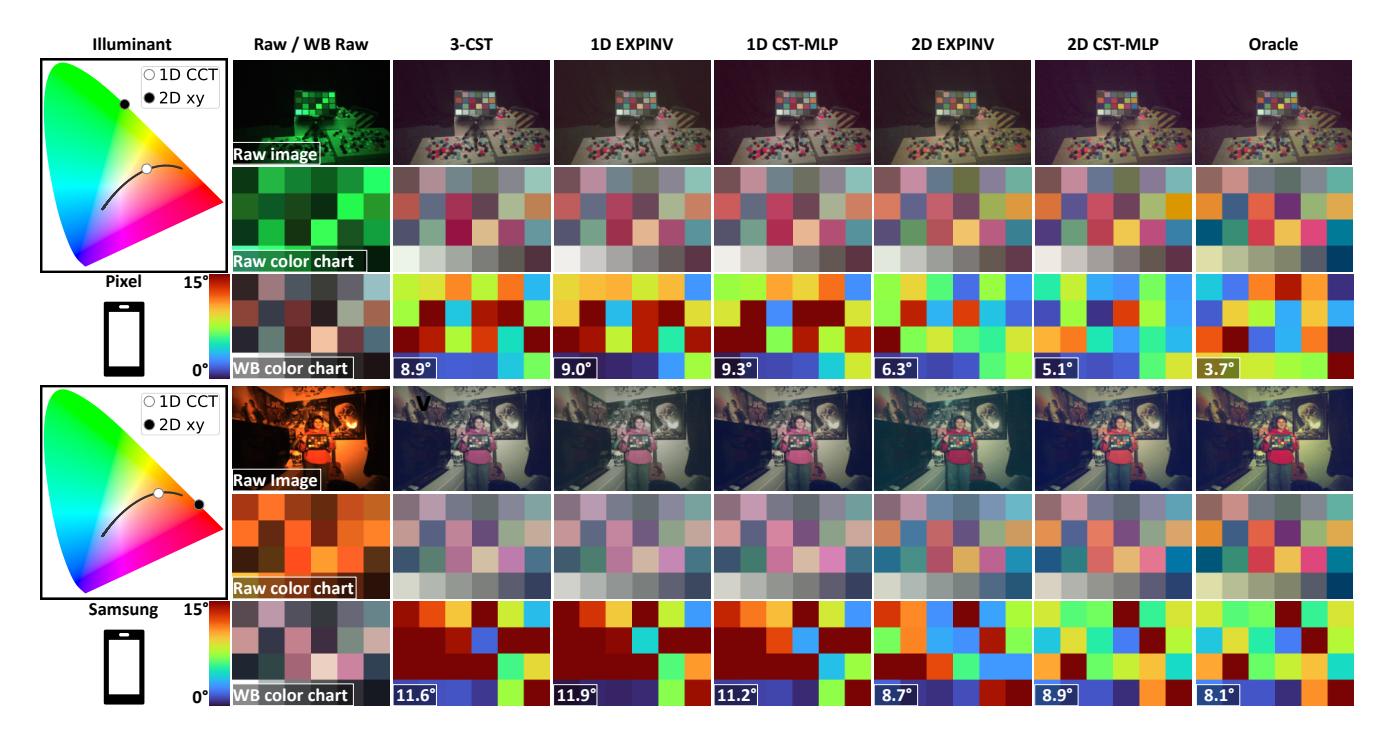


Figure 6. Colorimetric mapping results on in-the-wild captures. Results for two non-Planckian LED sources: green LED (top half) and orange LED (bottom half) illuminants, captured using Pixel and Samsung cameras. Each half starts with the illuminant's CCT and xy chromaticity and contains three rows: the top row shows raw-RGB image, and display-referred renderings; the middle row shows raw-RGB color chart and display-referred renderings; the bottom row shows white-balanced color chart and angular error maps. Methods: 3-CST [27], 1D EXPINV [33], 1D CST-MLP, 2D EXPINV [33], 2D CST-MLP, and Oracle. Key findings: (1) Our proposed 2D methods outperform 1D methods under in-the-wild lighting conditions. (2) Per-pixel methods such as EXPINV [33] can suffer from color casts.

4.3. LSMI Dataset Results

Finally, we evaluate CST-MLP on single-illuminant scenes and further extend it to mixed-illuminant scenes, both sourced from the LSMI [29] dataset.

Single-illuminant results. We train our CST-MLP and all baseline models on single-illuminant images from the LSMI dataset, since we do not have access to lightbox captures. We filter the LSMI dataset to include scenes where all patches on all color charts are not clipped, resulting in 1504 images for Galaxy and 1414 for Sony. We then split the data into train, validation, and test sets using 50%, 20%, and 30% of the images, respectively. For this method, we are unable to compare with CCCNN [38] and EXPINV [33] because these methods require access to the cameras' spectral sensitivities, which are not provided with the LSMI dataset. Summarized results comparing our 2D CST-MLP with 2-CST interpolation (using DNG CST matrices), nearest-neighbor (NN), and 1D CST-MLP baselines are presented in Table 3 (top). We find that our 2D CST-MLP achieves the highest performance on this dataset. Additional details and results are provided in Supplementary Section \$3.

		Single-	illuminan	t	
		Gal	laxy	So	ony
Method	Dim	Ang. (°)	ΔE_{2000}	Ang. (°)	ΔE_{2000}
Oracle	1D	2.38	4.90	1.59	3.52
2-CST [1]	1D	5.00	8.43	8.40	9.80
NN [44]	1D	4.46	7.40	3.07	5.19
CST-MLP	1D	3.77	6.30	2.70	4.55
NN [44]	2D	3.98	6.56	2.48	4.39
CST-MLP	2D	3.49	5.82	2.49	4.22
		Multi-	illuminant	;	
Oracle	1D	2.38	4.90	1.59	3.52
2-CST [1]	1D	5.00	8.43	8.40	9.80
NN [44]	1D	4.46	7.40	3.07	5.19
CST-MLP	1D	3.77	6.30	2.70	4.55
NN [44]	2D	3.98	6.56	2.48	4.39
CST-MLP	2D	3.49	5.82	2.49	4.22

Table 3. **LSMI results under single- and mixed-illuminant settings.** We compare our 2D chromaticity-based CST-MLP and NN [44] (highlighted blue) with baselines on Galaxy and Sony data from LSMI [29], reporting both angular error and ΔE_{2000} .

Multi-illuminant results. Assuming access to per-pixel illuminant information and blending maps that quantify

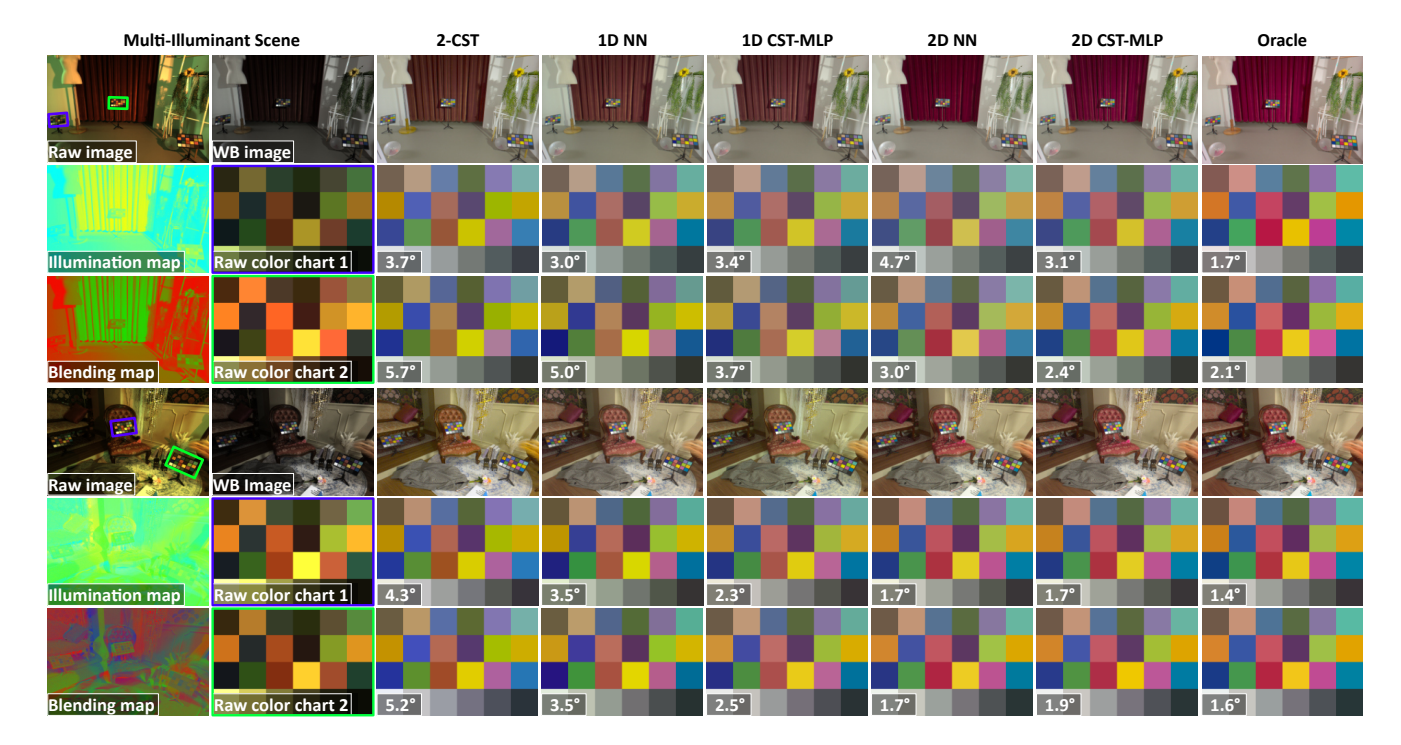


Figure 7. Colorimetric mapping results on spatially-varying multi-illuminant data from LSMI [29]. We visualize two multi-illuminant scenes from the Galaxy camera. Row structure for each half: Top row displays raw-RGB image, white-balanced raw-RGB image, and display-referred renderings; middle row shows contrast-stretched illumination map, first raw-RGB color chart, and display-referred renderings; bottom row presents blending map, second raw-RGB color chart, and display-referred renderings. Methods from left to right: 2-CST [1], 1D NN [44], 1D CST-MLP, 2D NN [44], 2D CST-MLP, and Oracle. Angular errors are displayed at the bottom left of each color chart image. Key findings: (1) Our 2D chromaticity-based methods can be extended to multi-illuminant scenes with knowledge of the illumination map and per-pixel blending maps. (2) Our 2D methods continue to exceed the performance of 1D counterparts.

each illuminant's contribution, we can apply our MLP trained on single-illuminant images to multi-illuminant scenes. Specifically, for each illuminant, we predict and apply the CST to the white-balanced image to generate multiple corrected versions. We then merge these corrected images using the blending map as weights. A detailed description of this procedure is provided in Supplementary Section S3. In Table 3 (bottom), we present quantitative comparisons of our method. Additionally, in Figure 7, we present qualitative results on 2- and 3-illuminant scenes from the LSMI dataset. We observe that our 2D CST-MLP outperforms other methods quantitatively and qualitatively, demonstrating the benefits of using a 2D chromaticity representation in multi-illuminant scenarios. Additional details and results are provided in Supplementary Section S3.

5. Conclusion

This paper demonstrates that shifting from conventional 1D CCT-based interpolation to 2D chromaticity-based neural prediction can improve in-camera colorimetric accuracy. Additionally, our investigation finds that using the 2D chromaticity space improves accuracy for all methods by cap-

turing illuminant characteristics that are lost in CCT parameterization. Moreover, our CST-MLP leverages this representation effectively while remaining lightweight and efficient. We demonstrate that our 2D CST-MLP outperforms existing methods on a newly introduced lightbox dataset, on in-the-wild scenes, and on both single- and mixed-illuminant data from the LSMI [29] dataset. Our approach has a computational cost nearly identical to current CCT-based interpolation methods, making it suitable for industry adoption and laying a foundation for next-generation camera color processing robust to illumination diversity.

Limitations and future work. We note that deriving xy chromaticity still depends on the DNG optimization procedure (Supplementary Section S5). Future work could remove this dependency and explore alternative chromaticity spaces better suited for this task. Next, like other colorimetric methods, our work is limited by metamers [36]—distinct spectra that produce identical camera responses. In our setting with LED illuminants, we observe increased metamers due to their narrow-band characteristics [49]. Please see Supplementary Section S1.5 for more discussion.

Off the Planckian Locus: Using 2D Chromaticity to Improve In-Camera Color

Supplementary Material

In Section S1, we present additional extensions, ablations, and limitations of our method. Sections S2–S4 include further results and details on our lightbox and in-the-wild datasets, the LSMI [29] dataset, and the NUS [10] dataset. Finally, Section S5 provides additional background on CCT-based interpolation and its implementation.

S1. Extensions and Additional Discussion

In this section, we elaborate on several key aspects of our method. We first detail an alternative data synthesis process for efficiently generating a large-scale laboratory dataset. Next, we describe the conversion of our MLP model into a computationally efficient look-up table (LUT) suitable for mobile deployment, and we add results utilizing alternative polynomial and root-polynomial mappings. We then present a series of ablation studies to analyze the impact of different architectural choices and conclude with a discussion on the limitations of our approach.

S1.1. Synthesizing Data

Cycling through all illuminants in the lightbox and capturing each image takes approximately 45 minutes per camera. However, we can speed up our capture process by using a simple technique that takes advantage of the linearity when capturing RAW sensor data [45]. The Telelumen lightbox mixes narrow-band LEDs to generate different SPDs. Similarly, we can simulate different camera responses by linearly combining raw images captured under individual LEDs as shown in Figure S1. Using this approach, we generated the full dataset and compared the results against training on real data. As shown in Figure S1, training the CST-MLP on simulated data resulted in only a negligible change in angular error, with a maximum difference of 0.06° .

Simulation details. Formally, our lightbox contains 7 narrow-band LEDs, each with a spectral power distribution (SPD) denoted by $L_i(y)$, where $i \in [0,7]$. We capture 7 images I^i of the color chart, each illuminated by a single LED $i \in [1,7]$ with intensity α_i , where $\alpha_i = 0$ indicates the LED is off and $\alpha_i = 1$ indicates maximum brightness. The simulated spectra in the lightbox is given by

$$L_t(y) = \sum_{i=0}^{7} \alpha_i L_i(y).$$
 (S2)

Under the traditional image formation model, the raw image I at a location x is given by

$$I_t(x) = \int_{\mathcal{X}} L(y)R(x,y)S(x,y)\,dy,\tag{S3}$$

where R(x,y) is the scene reflectance, and S(x,y) is the sensor sensitivity. The raw color response is given by integrating across all wavelengths y in the visible range γ .

We can now substitute the definition provided in Equation S2 into the image formation model given in Equation S3,

$$I_{sim}(x) = \int_{\gamma} \left(\sum_{i=0}^{7} \alpha_i L_i(y) \right) R(x, y) S(x, y) dy$$

$$= \sum_{i=0}^{7} \alpha_i \int_{\gamma} L_i(y) R(x, y) S(x, y) dy$$

$$= \sum_{i=0}^{7} \alpha_i I_i(x),$$
(S4)

showing the lightbox image is equivalent to a weighted combination of the individual LED images. We note that sensor effects such as noise are not captured under this model, however, we capture at a low noise level (ISO 100).

S1.2. Look-Up-Table (LUT) Conversion

Our 2D CST-MLP can be converted into a look-up-table (LUT), enabling CST prediction on mobile devices without evaluating the MLP. We perform this conversion by uniformly sampling the MLP with a 2D grid and storing the predicted CST at each location. At test time, given a 2D chromaticity coordinate, we utilize bilinear interpolation to generate the output CST. We try various LUT sizes, as shown in Table S1, and find that a 20×20 LUT that uses 14 KB is nearly identical to our MLP's performance. We note that the MACs remain identical across all methods because the dominant computational cost is in applying the predicted CST rather than computing it.

S1.3. Polynomial/Root-Polynomial Mappings

Prior work in color correction has explored polynomial and root-polynomial mappings [19, 24]. These methods expand the traditional 3×3 transformation into higher-order feature spaces to enable more expressive mapping at the cost of larger model size and a non-invertible transformation. In Table S2, we evaluate the performance of our 2D CST MLP when predicting linear, polynomial, and root-polynomial mappings. Root-polynomial mappings outperform all other

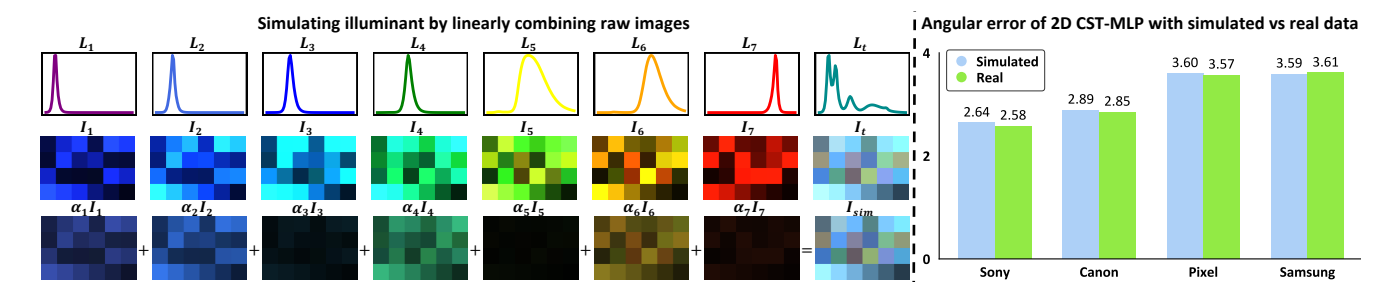


Figure S1. Validation of the RAW data synthesis pipeline. Left: A schematic of the simulation process, where a novel RAW image response I_{sim} under a target illuminant L_t is synthesized by linearly combining 7 pre-captured RAW images I_i , each illuminated by a single narrow-band LED L_i . The weights α_i correspond to the contribution of each LED required to create the target spectral power distribution. Right: A bar chart validating this approach by comparing the mean angular error of the 2D CST-MLP model when trained on data from the synthesis pipeline *Simulated* versus data captured sequentially under each illuminant *Real*. The nearly identical performance across all four camera sensors (Sony, Canon, Pixel, Samsung) confirms the validity of the data synthesis technique, enabling the rapid generation of a large-scale, off-locus illuminant dataset.

	Sizo	MACs	Lightl	юх	In-the-	wild
Method	(KB)	(M)	Ang. (°)	ΔE	Ang. (°)	ΔE
2D CST-MLP	1.54	0.01	3.57	7.91	4.47	8.29
$10 \times 10 \text{ LUT}$	3.52	0.01	3.80	8.37	4.53	8.33
$20\times20~\mathrm{LUT}$	14.06	0.01	3.57	7.98	4.43	8.24

Table S1. Converting 2D CST-MLP into LUTs. We convert our 2D CST-MLP trained on the Pixel camera dataset into LUTs of different resolutions and find that a small 20×20 LUT is comparable in performance to our 2D CST-MLP.

models on both angular error (°) and ΔE_{2000} on the in-the-wild dataset. On the lightbox dataset, root-polynomial mappings achieve the smallest ΔE_{2000} , while polynomial mappings obtain the lowest angular error (°) but fail to generalize to in-the-wild capture data. This behavior is likely a consequence of the polynomial mapping overfitting to particular exposure values [19]. Expanded root-polynomial mappings result in lower mean angular error, and could be used in place of the linear mappings of the DNG [1] standard if invertibility is not a requirement.

	Size	Ligh	tbox	In-the	e-wild
Method	(KB)	Ang. (°)	ΔE_{2000}	Ang. (°)	ΔE_{2000}
Linear (3×3)	1.54	3.57	7.91	4.47	8.29
Poly (3×9)	3.86	3.08	9.32	4.69	10.22
Poly (3×19)	7.72	2.70	11.77	4.90	12.37
R-poly (3×6)	2.70	3.27	7.74	4.11	8.14
R-poly (3×13)	5.40	3.29	7.79	4.29	8.53

Table S2. Quantitative evaluation of polynomial and root-polynomial methods. We evaluate the performance of methods trained with 2D chromaticity input when predicting linear, polynomial (Poly), and root-polynomial (R-poly) [19, 24] mappings. For both polynomial and root-polynomial mappings, we test with two different kernel sizes.

S1.4. Ablations

This section presents a series of ablation studies. We begin by comparing compare our model's performance to baseline methods across different input types and examine performance under varying levels of noise. We also assess the impact of network architecture modifications on our proposed method. Finally, we evaluate both our model and the baselines under controlled perturbations of the white point input.

Input coordinate ablation. We evaluate the performance of our method using three different coordinate types: 1D (CCT), 2D (raw), and 2D (xy) in Table S3. Our results indicate that the 2D xy chromaticity space is the most informative, consistently improving performance across all models. Furthermore, we observe that our noise augmentation improves generalization to in-the-wild illuminants, while direct pixel-prediction methods show a decline in performance under the same augmentation.

Noise augmentation ablation. We evaluate our CST-MLP method across varying levels of input noise applied during training and find that utilizing higher noise levels improves generalization to in-the-wild scenes at the cost of reduced accuracy on the original lightbox illuminants. Table S4 presents these results, highlighting the importance of our noise augmentation for generalization.

Nodes and layers ablation. We conduct a detailed ablation study to determine the effect of our MLP's architecture on its performance. In this study, we vary the number of nodes per layer from 8 to 256 and the number of hidden layers from 1 to 3. The comprehensive results, including both angular error and ΔE_{2000} for the Sony, Canon, Pixel, and Samsung cameras, are presented in Table S6.

The results show that performance is remarkably consistent across different network sizes. While larger models with more nodes and layers occasionally yield marginal improvements, these gains are not significant enough to justify the increase in model complexity. Given this trade-off between size and performance, we adopt the single-layer, 32-node architecture for all our experiments, as it provides a strong balance of efficiency and accuracy.

White balance error ablation. In the main paper, we assume that the ground-truth illuminant is known to isolate the performance of various CST prediction methods. In practice, however, this assumption does not hold as white-balance estimation [3, 31] modules are imperfect.

To better assess real-world performance with imperfect white points, we test our method (trained with ground truth white points) alongside several baselines on the lightbox dataset with controlled white-point offsets (Table S5). For each chart, we shift the white point by sampling a random direction and applying an offset of 0° , 1° , 2° , or 3° . Our results show that CST-MLP achieves the lowest mean angular error when the whitepoint is offset by $0^{\circ} - 2^{\circ}$, which falls within the typical range of white-point estimators such as CCMNet [31] and Time-Aware White Balance [3] which achieve $1.01^{\circ} - 2.23^{\circ}$ mean and $0.60^{\circ} - 1.71^{\circ}$ median angular error. We note that when the white-point offset is large (3°), our 2D CST-MLP performs similarly to 1D CST-MLP, but still outperforms 2-CST traditional interpolation.

S1.5. Limitations

Metamers, unique spectral distributions that produce identical camera responses, pose a fundamental challenge for all color constancy methods [36]. They arise naturally from projecting continuous spectral power distributions into three-channel color spaces [53]. This phenomenon is especially pronounced under narrow-band or highly saturated illuminants, where the limited range of reflected wavelengths increases the likelihood that distinct spectra produce identical camera responses [49]. This makes metamerism a source of ambiguity that can not be resolved with traditional color constancy techniques [36]. An illustration of this behavior can be seen in Figure S2.

S2. Our Lightbox and In-The-Wild Dataset

We provide additional descriptions and results on our lightbox and in-the-wild dataset. Additionally, please see the supplementary material for a montage of the raw captures from these datasets.

S2.1. Dataset Details

Lightbox dataset. The lightbox dataset contains 790 illuminants sourced from two datasets. The first consists of

	Input	Nio.	Ligh	tbox	In-th	e-wild
Method	coord.	Noise aug.	Ang. (°)	ΔE_{2000}	Ang. (°)	ΔE_{2000}
	1D (CCT)	Х	4.03	8.35	4.86	8.48
	2D (raw)	X	3.58	7.99	5.39	9.64
CST-MLP	2D (raw)	✓	3.70	7.91	4.92	8.79
	2D (xy)	X	3.53	7.92	5.04	9.12
	2D (xy)	✓	3.57	7.91	4.47	8.29
	1D (CCT)	Х	4.41	8.30	4.87	8.54
	2D (raw)	X	3.90	7.92	4.69	8.40
CCCNN	2D (raw)	✓	4.18	7.91	4.44	7.88
	2D (xy)	X	4.00	8.07	4.63	8.19
	2D (xy)	✓	4.14	8.08	4.51	8.14
	1D (CCT)	Х	4.29	8.18	4.91	8.50
	2D (raw)	Х	3.78	7.77	4.33	7.80
EXPINV	2D (raw)	✓	4.24	8.12	4.44	7.92
	2D (xy)	X	3.84	7.77	4.35	7.97
	2D (xy)	✓	3.96	8.11	4.39	8.05

Table S3. Ablation of input coordinates. We evaluate the performance of our CST-MLP as well as the CCCNN and EXPINV methods using 1D and 2D input coordinates with a noise augmentation level of $\sigma=0.05$. Results shows us that our CST-MLP performs best with 2D chromaticity input.

	Noise aug.	Lighth	ox	In-the-v	vild
Method	level (σ)	Ang. (°)	ΔE	Ang. (°)	ΔE
	0.00	3.53	7.92	5.04	9.12
CST-MLP	0.05	3.57	7.91	4.47	8.29
CS1-MILP	0.10	3.80	8.17	4.26	7.89
	0.20	3.97	8.33	4.55	8.25

Table S4. **Ablation of noise augmentation.** We evaluate the performance of the 2D CST-MLP using xy chromaticity input on the Pixel camera lightbox dataset under varying noise augmentation levels applied during training.

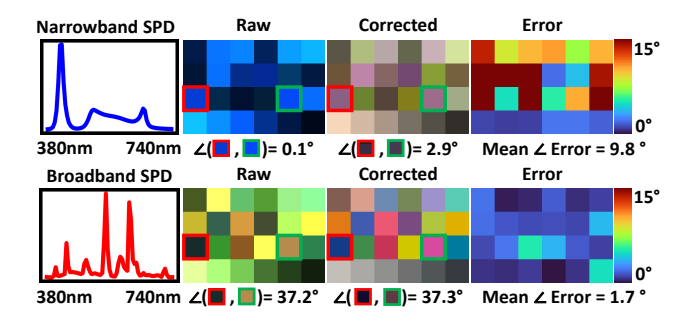


Figure S2. Limitations from metameric sensor responses. Metamers are distinct spectral distributions that produce identical camera responses. Metamers can occur under all illuminants, but are more common under narrowband illumination (top). In this scenario, two patches with different reflectances (highlighted in red and green) yield nearly identical raw responses, resulting in colorimetric failure for our 2D CST-MLP. Although our method fails, this is an inherent limitation for all color constancy methods [36]. Color differences are quantified using angular error.

		Offse	et: 0°	Offs	et: 1°	Offse	et: 2°	Offs	et: 3°
Method	Input coord.	Ang. (°)	ΔE_{2000}						
2-CST [1]	1D (CCT)	4.56	9.18	5.08	9.80	6.28	11.30	7.87	13.16
3-CST [27]	1D (CCT)	4.53	9.16	5.05	9.78	6.25	11.27	7.84	13.13
CCCNN [38]	1D (CCT)	4.41	8.30	4.93	9.10	5.91	10.62	7.13	12.31
CCCNN [38]	2D (xy)	4.00	8.07	4.68	8.86	5.86	10.41	7.27	12.20
EXPINV [33]	1D (CCT)	4.29	8.18	4.88	9.05	5.98	10.67	7.32	12.42
EXPINV [33]	2D (xy)	3.84	7.77	4.62	8.70	5.95	10.40	7.40	12.23
NN [44]	1D (CCT)	6.65	11.72	6.07	10.75	6.65	11.72	7.90	13.44
NN [44]	2D (xy)	4.25	8.75	5.27	9.94	7.03	12.03	9.15	14.33
CST-MLP	1D (CCT)	4.03	8.35	4.61	9.17	5.86	10.86	7.46	12.82
CST-MLP	2D (xy)	3.57	7.91	4.30	8.82	5.76	10.61	7.54	12.64

Table S5. Quantitative evaluation of methods under varying white point perturbations. We evaluate the performance of 2-CST, 3-CST, CCCNN, EXPINV, NN, and CST-MLP with 1D and 2D xy chromaticity inputs on varying degrees of white point offsets. The angular offset columns show the angular offset added to each white point during testing. White points are shifted by sampling a random direction and applying the corresponding offset. The results show that our CST MLP is the best-performing method in the $0^{\circ} - 2^{\circ}$ error range, and that all methods are comparable under large white-point errors (3°). Methods using 2D xy chromaticity inputs are highlighted in blue.

			Angular Error (°)																			
					Sony	,			(Cano	n				Pixe	l			S	amsu	ng	
Nodes	Layers	Size (KB)	Mean	25%	50%	75%	90%	Mean	25%	50%	75%	90%	Mean	25%	50%	75%	90%	Mean	25%	50%	75%	90%
8	1	0.41	2.70	0.78	1.68	3.47	6.31	3.24	1.03	1.98	4.15	7.56	3.83	1.32	2.52	4.91	8.67	3.80	1.30	2.47	4.93	8.64
8	2	0.69	2.65	0.80	1.69	3.39	6.20	2.93	0.87	1.91	3.84	6.76	3.69	1.28	2.41	4.65	8.30	3.70	1.26	2.42	4.70	8.38
8	3	0.97	2.66	0.81	1.71	3.45	6.14	2.96	0.89	1.89	3.81	6.80	3.63	1.25	2.42	4.59	8.28	3.70	1.26	2.45	4.65	8.46
16	1	0.79	2.73	0.86	1.73	3.45	6.33	2.93	0.87	1.84	3.80	6.64	3.65	1.19	2.41	4.64	8.30	3.68	1.24	2.43	4.70	8.46
16	2	1.85	2.65	0.83	1.72	3.41	6.08	2.88	0.87	1.85	3.80	6.59	3.59	1.19	2.41	4.62	8.04	3.64	1.20	2.45	4.59	8.23
16	3	2.91	2.64	0.85	1.68	3.34	6.00	2.88	0.85	1.83	3.75	6.59	3.60	1.24	2.39	4.58	8.20	3.61	1.24	2.38	4.53	8.2
32	1	1.54	2.66	0.82	1.70	3.41	6.14	2.89	0.87	1.85	3.75	6.67	3.60	1.22	2.38	4.60	8.18	3.60	1.20	2.43	4.56	8.23
32	2	5.66	2.63	0.83	1.70	3.38	5.98	2.94	0.84	1.87	3.77	6.79	3.56	1.17	2.35	4.64	7.99	3.60	1.19	2.40	4.54	8.28
32	3	9.79	2.65	0.84	1.72	3.40	6.00	2.85	0.84	1.80	3.70	6.56	3.73	1.25	2.39	4.56	8.21	3.68	1.24	2.43	4.53	8.16
64	1	3.04	2.66	0.85	1.72	3.42	6.09	2.89	0.86	1.86	3.80	6.78	3.58	1.20	2.45	4.63	7.98	3.60	1.21	2.48	4.58	8.12
64	2	19.29	2.62	0.82	1.64	3.34	6.11	2.89	0.83	1.80	3.78	6.74	3.55	1.26	2.39	4.54	7.88	3.64	1.24	2.44	4.49	8.05
64	3	35.54	2.65	0.82	1.68	3.38	6.06	2.89	0.85	1.82	3.75	6.74	3.63	1.20	2.39	4.57	8.13	3.52	1.20	2.37	4.44	7.87
128	1	6.04	2.64	0.84	1.68	3.37	6.09	2.88	0.83	1.83	3.76	6.74	3.57	1.19	2.42	4.59	7.90	3.64	1.23	2.43	4.49	8.2
128	2	70.54	2.64	0.84	1.63	3.34	6.14	2.88	0.84	1.81	3.73	6.69	3.56	1.24	2.44	4.55	7.83	3.56	1.23	2.45	4.51	8.00
128	3	135.04	2.67	0.81	1.69	3.41	6.10	2.89	0.85	1.82	3.79	6.67	3.56	1.25	2.35	4.55	8.03	3.55	1.25	2.42	4.46	7.85
												Δ	E_{2000}									
8	1	0.41	6.67	3.55	5.96	8.84	11.55	7.61	4.14	6.67	9.59	13.68	8.30	5.05	7.44	10.79	14.16	7.96	4.50	7.42	10.11	13.7
8	2	0.69	6.65	3.57	5.95	8.76	11.49	7.32	4.01	6.46	9.38	12.85	8.09	4.71	7.29	10.57	13.62	7.87	4.36	7.32	10.14	13.3
8	3	0.97	6.74	3.71	6.03	8.81	11.66	7.31	4.04	6.46	9.35	12.85	8.02	4.77	7.29	10.39	13.33	7.84	4.43	7.33	10.11	13.3
16	1	0.79	6.71	3.64	5.91	8.82	11.60	7.24	3.95	6.43	9.33	12.76	8.04	4.88	7.28	10.49	13.50	7.79	4.37	7.30	10.05	13.3
16	2	1.85	6.65	3.58	6.05	8.81	11.39	7.12	3.96	6.35	9.22	12.56	7.96	4.84	7.21	10.26	13.34	7.76	4.34	7.26	10.01	12.9
16	3	2.91	6.69	3.65	5.96	8.78	11.23	7.17	4.02	6.45	9.27	12.63	7.97	4.72	7.31	10.25	13.40	7.75	4.31	7.29	10.01	12.9
32	1	1.54	6.73	3.66	6.07	8.85	11.58	7.17	3.96	6.41	9.28	12.55	7.95	4.78	7.21	10.40	13.26	7.74	4.38	7.29	10.05	13.1
32	2	5.66	6.60	3.66	5.94	8.69	11.37	7.24	4.06	6.43	9.19	12.69	7.90	4.78	7.22	10.25	13.19	7.70	4.35	7.26	9.96	13.0
32	3	9.79	6.78	3.73	6.15	8.88	11.60	7.16	3.97	6.42	9.28	12.62	8.18	4.80	7.20	10.30	13.36	7.88	4.34	7.32	9.99	12.9
64	1	3.04	6.66	3.62	5.96	8.82	11.51	7.20	3.96	6.41	9.24	12.63	7.99	4.86	7.23	10.41	13.29	7.77	4.49	7.27	9.98	13.0
64	2	19.29	6.60	3.54	5.92	8.78	11.48	7.14	3.90	6.42	9.22	12.63	7.94	4.79	7.22	10.28	13.17	7.80	4.43	7.30	9.90	12.7
64	3	35.54	6.69	3.69	6.01	8.78	11.49	7.19	4.04	6.47	9.27	12.64	8.00	4.74	7.18	10.28	13.28	7.57	4.40	7.24	9.78	12.6
128	1	6.04											7.92									
128	2	70.54											7.94									
128	3	135.04						7.20														

Table S6. **Ablation of CST-MLP with varying node and layer sizes.** Our 2D CST-MLP with xy chromaticity input and noise augmentation is evaluated on camera data from lightbox scenes with varying node and layer counts. Our chosen configuration (highlighted in blue) uses 32 nodes and one layer, and is lightweight yet still competitive in performance.

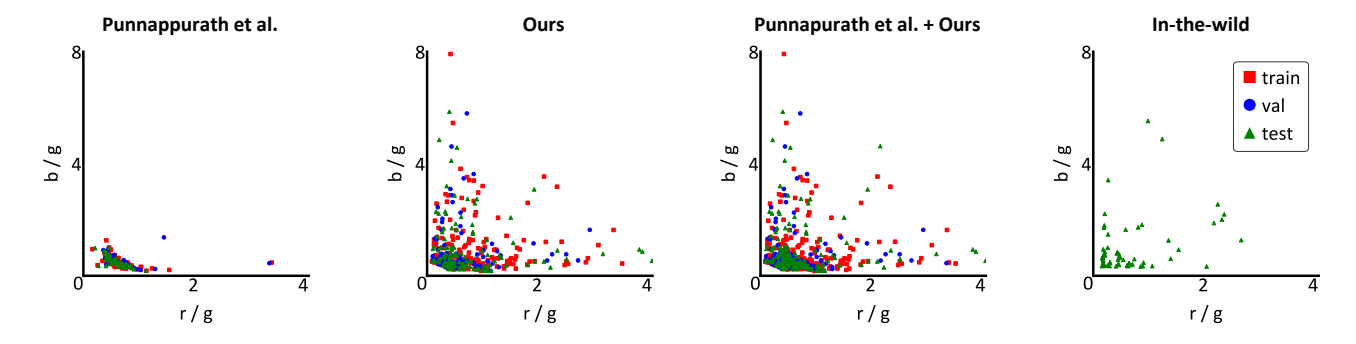


Figure S3. We visualize the chromaticities of four illuminant sets: those from Punnapurath et al. [45], those we sample from a Dirichlet distribution, the combined training set (Punnapurath et al. and ours), and the in-the-wild testing set. Our lightbox illuminants span a broader chromaticity region that contains the in-the-wild illuminants.

390 real illuminants from Punnappurath et al. [45], with 190 training, 78 validation, and 117 test samples as originally defined. The second source comprises 400 synthetic illuminants generated by linearly combining the seven Telelumen illuminant SPDs. We generate these illuminants by sampling 400 seven-dimensional weight vectors from a Dirichlet distribution [17], where each element of a vector corresponds to the contribution of one illuminant to the synthetic SPD. To reduce bias toward clustered LEDs, the Dirichlet concentration parameters are adjusted and normalized to sum to 1, ensuring that the illuminants span a larger portion of the raw chromaticity space, as seen in Figure S3. These weighted vectors are then used to compute the final synthetic illuminants via a linear combination of the lightbox LED illuminant SPDs. Finally, we split the synthetic dataset into 200 training, 80 validation, and 120 test illuminants. We combine both datasets, resulting in 395 training, 158 validation, and 237 test illuminants. Please see the supplementary montage for a preview of the raw images.

S2.2. Data capture

In-the-wild dataset. As described in the main paper, we further evaluated our method on a small in-the-wild dataset captured using mobile phones (Pixel and Samsung). We captured images with ISO level 50 on Samsung and 21 on Pixel as well as using low exposure to ensure that no color patches were clipped. Our final dataset consists of 64 images from each camera, captured under identical scenes and lighting conditions.

S2.3. Additional Results

Lightbox dataset. We provide additional qualitative results for all cameras in our lightbox dataset in Figure S4. Our method generalizes well across a wide range of illuminants, and 2D chromaticity-based approaches consistently outperform 1D inputs.

In-the-wild dataset. Our 2D CST-MLP generalizes well to various in-the-wild scenes as can be seen qualitatively in Figures S5-S6 and quantitatively in Table S7. CST-MLP performs worse than our proposed 2D EXPINV variant on color chart evaluations in the wild. However, we observe that EXPINV often introduces color casts in full-size images, likely because it is a spatially varying per-pixel transform that doesn't enforce global consistency. Please see the supplementary montage to view the raw captured images.

S3. LSMI Dataset

In this section, we provide an overview of the LSMI dataset and the preprocessing steps we utilized. We then explain how we extend CST-MLP to multi-illuminant scenes using blending maps and present complementary quantitative and qualitative results.

S3.1. Dataset Details

The Large-Scale Multi-Illuminant (LSMI) dataset [29] comprises 2,700 scenes captured using a Samsung Galaxy Note 20 Ultra (Galaxy), Sony $\alpha 9$ (Sony), and Nikon D810 (Nikon). Each scene contains multiple color charts and two or three distinct illuminants, covering both natural and indoor conditions. Each scene provides both single- and multi-illuminant images, enabling evaluation of algorithms under controlled and complex lighting scenarios.

Data processing. To enable evaluation, we process the scenes and organize the dataset, ensuring consistency across all splits. We extract the color chart values following the procedure detailed in Section 3.2 of the main paper, using a smaller 3×3 pixel region to accommodate small color charts that are far from the camera. We then partition the dataset by scene, ensuring that each scene is assigned to the training, validation, or testing sets to prevent leakage between splits. These same splits are maintained across single- and multi-illuminant experiments.

							An	gular	Erro	(°)			
			MACs			Pixe	l			S	amsu	ng	
Method	Dim	(KB)	(M)	Mean	25%	50%	75%	90%	Mean	25%	50%	75%	90%
Oracle	1D	0.00	0.01	2.65	0.80	1.77	3.39	5.92	2.75	0.75	1.77	3.45	6.28
2-CST [1]	1D	0.07	0.01	5.04	1.60	3.95	7.11	10.94	5.09	1.75	3.95	6.94	10.95
3-CST [27]	1D	0.11	0.01	5.03	1.61	3.92	7.07	10.94	5.11	1.75	3.98	6.92	11.03
NN [44]	1D	15.43	0.01	6.19	2.02	4.85	8.60	13.31	5.70	2.01	4.27	7.79	12.45
CCCNN [38]	1D	68.51	13.39	4.87	1.70	3.66	6.78	10.56	5.02	1.72	3.67	6.92	10.79
EXPINV [33]	1D	68.53	13.39	4.91	1.71	3.67	6.83	10.49	4.77	1.46	3.44	6.74	10.67
CST-MLP	1D	1.41	0.01	4.86	1.61	3.63	6.78	10.80	4.87	1.57	3.57	6.70	10.74
NN [44]	2D	16.97	0.01	6.55	1.96	4.63	8.54	14.43	8.90	2.85	5.88	10.89	22.99
CCCNN [38]	2D	69.01	13.48	4.63	1.57	3.44	6.42	10.08	4.51	1.62	3.42	6.26	9.63
EXPINV [33]	2D	69.03	13.48	4.35	1.47	3.19	6.00	9.45	4.58	1.67	3.37	6.40	9.95
CST-MLP	2D	1.54	0.01	4.47	1.47	3.43	6.19	10.08	4.46	1.48	3.23	6.01	9.94
								ΔE	2000				
Oracle	1D	0.00	0.01	5.80	3.03	4.80	7.43	10.65	5.84	2.96	4.83	7.39	10.91
2-CST [1]	1D	0.07	0.01	8.79	4.69	7.47	10.97	15.64	8.82	4.75	7.49	11.01	14.87
3-CST [27]	1D	0.11	0.01	8.79	4.68	7.44	10.97	15.50	8.84	4.79	7.52	11.01	15.04
NN [44]	1D	15.43	0.01	10.52	5.31	8.57	13.33	19.87	9.83	5.44	8.20	12.02	17.61
CCCNN [38]	1D	68.51	13.39	8.54	4.63	7.16	10.69	15.63	8.55	4.76	7.25	10.58	15.11
EXPINV [33]	1D	68.53	13.39	8.50	4.56	7.18	10.49	15.60	8.35	4.55	7.01	10.60	14.71
CST-MLP	1D	1.41	0.01	8.48	4.32	7.10	10.59	15.65	8.47	4.52	6.94	10.28	15.23
NN [44]	2D	16.97	0.01	11.04	5.24	8.56	14.21	22.22	13.91	7.31	11.35	17.56	28.61
CCCNN [38]	2D	69.01	13.48	8.19	4.32	6.80	10.41	15.19	8.03	4.23	6.56	10.49	15.37
EXPINV [33]	2D	69.03	13.48	7.97	4.15	6.70	10.03	15.23	8.18	4.45	7.23	10.39	14.77
CST-MLP	2D	1.54	0.01	8.29	4.29	6.85	10.61	15.30	8.16	4.45	6.74	9.90	14.58

Table S7. Qualitative evaluation of in-the-wild dataset. We compare angular error and ΔE_{2000} of traditional 2-CST/3-CST interpolation [1, 27], NN [44], CCCNN [38], EXPINV [33], and our proposed CST-MLP. For NN, CCCNN, EXPINV, and CST-MLP, we evaluate both 1D CCT-based and 2D chromaticity-based variants (highlighted in blue). We find using 2D chromaticity coordinates leads to lower error for all methods.

Single-illuminant data. The single-illuminant subset is constructed from the multi-illuminant captures of each scene by applying pairwise subtraction, allowing recovery of multiple single-illuminant images per scene. We discard images with color charts containing pixels with near-zero or maximum white-level values. Applying this procedure yields 1,504 images from the Galaxy, 720 from the Nikon, and 1,414 from the Sony. Each camera's images are then split into training, validation, and test sets following the previously described partitioning, resulting in splits of 449/756/299 for Galaxy, 360/142/218 for Nikon, and 709/283/422 for Sony.

Multi-illuminant data. To build the multi-illuminant subset, we apply the same quality-filtering criteria used in the single-illuminant subset. Each scene provides perpixel illuminant maps $W \in \mathbb{R}^{H \times W \times 2}$ and blending maps $B_i \in \mathbb{R}^{H \times W}$ where B_i encodes the spatial contribution of illuminant i to the final image. Using the same scene splits, we build the training, validation, and test sets. For the Galaxy, this results in 358/143/216 images; for the Nikon, 176/70/106; and for the Sony, 325/130/195.

S3.2. Applying CST-MLP to Multi-Illuminant Scenes

We train CST-MLP on single-illuminant scenes and apply it to multi-illuminant scenes given the raw image, illumination map, and blending maps. We assume all illumination information is known, because our work, CST-MLP, focuses only on the CST stage of the colorimetric mapping process.

First, we compute the white-balanced image I_{wb} by performing a per-pixel diagonal correction of the raw image using the illumination map W. Given the white point w_i (derived from the white patch of the single-illuminant image under illumination i), we then compute the corresponding CST T_i using our CST-MLP. The final corrected color at a pixel x is obtained by blending the per-illuminant transformations:

$$I_{xyz}(x) = I_{wb}(x) \sum_{i} B_i(x) T_i, \tag{S5}$$

where each CST T_i contributes proportionally to its blending weight B_i . This formulation requires a per-pixel CST to be computed and applied, which is computationally expensive. To reduce computation, we adopt an equivalent formulation that applies each illuminant's CST globally to

							Si	ngle-I	llumir	nant								
										Angu	lar E	rror (°	")					
		Size	MACs		(Galax	ку				Sony	,				Nikoi	1	
Method	Dim	(KB)	(M)	Mean	25%	50%	75%	90%	Mean	25%	50%	75%	90%	Mean	25%	50%	75%	90%
Oracle	1D	0.00	0.01	2.38	0.61	1.33	2.73	5.30	1.59	0.55	1.10	2.06	3.40	1.37	0.48	0.96	1.79	3.00
2-CST [1]	1D	0.07	0.01	5.00	2.11	4.15	6.07	9.24	8.40	3.78	8.77	12.27	15.22	8.16	3.91	8.49	11.81	14.65
NN [44]	1D	29.53	0.01	4.46	1.61	3.20	5.65	9.24	3.07	1.13	2.11	3.81	6.47	3.27	1.16	2.21	4.16	7.23
CST-MLP	1D	1.41	0.01	3.77	1.19	2.36	4.76	8.49	2.70	0.97	1.82	3.51	5.81	2.57	0.90	1.71	3.19	5.90
NN [44]	2D	32.48	0.01	3.98	1.30	2.60	4.97	8.65	2.48	0.94	1.77	3.17	5.36	3.06	1.05	2.07	3.99	6.56
CST-MLP	2D	1.54	0.01	3.49	1.11	2.20	4.31	7.45	2.49	0.90	1.68	3.15	5.34	2.48	0.85	1.62	3.04	5.65
											ΔE_{20}	000						
Oracle	1D	0.00	0.01	4.90	2.13	3.55	5.80	9.52	3.52	1.82	2.92	4.56	6.59	3.36	1.74	2.80	4.24	6.36
2-CST [1]	1D	0.07	0.01	8.43	4.01	6.60	10.89	15.51	9.80	6.55	10.46	12.95	15.41	9.63	6.73	10.30	12.63	14.75
NN [44]		29.53	0.01	7.40	3.46	5.54	9.01	14.61	5.19	2.69	4.11	6.19	9.16	5.31	2.78	4.25	6.72	9.80
CST-MLP	1D	1.41	0.01	6.30	2.76	4.42	7.40	12.78	4.55	2.37	3.57	5.39	8.08	4.42	2.29	3.48	5.49	8.35
NN [44]	2D	32.48	0.01	6.56	3.08	4.91	7.90	12.57	4.39	2.36	3.71	5.61	8.04	5.25	2.65	4.16	6.50	9.97
CST-MLP	2D	1.54	0.01	5.82	2.67	4.21	6.89	11.17	4.22	2.24	3.40	5.12	7.47	4.33	2.25	3.40	5.41	8.12
							M	[ulti-I]	lumin	ant								
										Angu	lar E	rror (°	")					
		Size	MACs		(Galax	ку				Sony	,				Nikoi	1	
Method	Dim	(KB)	(M)	Mean	25%	50%	75%	90%	Mean	25%	50%	75%	90%	Mean	25%	50%	75%	90%
Oracle	1D	0.00	0.01	2.06	0.79	1.49	2.65	4.17	1.44	0.60	1.11	1.90	2.91	1.45	0.60	1.08	1.89	2.96
2-CST [1]	1D	0.07	0.01	3.88	1.76	3.49	5.38	7.12	8.14	3.64	8.51	12.11	14.49	7.87	3.66	8.26	11.56	14.01
NN [44]	1D	29.53	0.01	3.23	1.32	2.47	4.18	6.52	2.43	0.97	1.73	3.00	5.12	2.58	1.01	1.83	3.32	5.55
CST-MLP	1D	1.41	0.01	2.52	0.97	1.79	3.16	5.20	1.88	0.79	1.41	2.47	3.87	1.86	0.77	1.46	2.40	3.70
NN [44]	2D	32.48	0.01	2.83	1.10	2.10	3.67	5.69	1.93	0.82	1.46	2.44	3.91	2.25	0.91	1.65	2.83	4.65
CST-MLP	2D	1.54	0.01	2.26	0.88	1.61	2.82	4.68	1.82	0.79	1.39	2.32	3.64	1.77	0.73	1.34	2.24	3.63
											ΔE_{20}	000						
Oracle	1D	0.00	0.01	3.92	2.14	3.19	4.69	6.63	3.01	1.77	2.64	3.78	5.17	2.99	1.72	2.59	3.71	5.16
2-CST [1]	1D	0.07	0.01	6.87	3.31	5.20	9.62	13.50										13.67
NN [44]		29.53	0.01				6.63	9.81			3.42	5.05	7.37	4.22			5.17	7.65
CST-MLP		1.41	0.01				4.96	7.60				4.13	5.72		1.94		4.04	5.81
NN [44]		32.48					5.66	8.14			3.12		6.18			3.34		7.02
CST-MLP		1.54	0.01					6.61			2.82			3.24			3.88	

Table S8. Quantitative evaluation on LSMI dataset. We compare 2-CST [1] and NN [44] methods against our proposed CST-MLP using angular error and ΔE_{2000} on single- and multi-illuminant scenes. Methods using 2D chromaticity inputs are highlighted in blue.

the white-balanced image and blends the results:

$$I_{xyz} = \sum_{i} B_i [I_{wb} T_i]. \tag{S6}$$

We adopt this formulation for our method and all baselines.

S3.3. Additional Results

We present a comprehensive evaluation of our proposed CST-MLP method on the LSMI dataset, comparing it with traditional 2-CST [1] interpolation and NN [44] across both single- and multi-illuminant scenarios. The results, summarized in Table S8, demonstrate the effectiveness of our approach using both traditional 1D and our proposed 2D chromaticity input. Performance is quantified using both angular error and ΔE_{2000} .

For a more detailed and qualitative analysis, we provide a series of visual comparisons. Figures S7-S9 showcase the colorimetric mapping results on the single-illuminant subset of the LSMI dataset for the Sony, Galaxy, and Nikon cameras, respectively. These figures illustrate the qualitative impact of our method on color accuracy.

Similarly, Figures S10-S12 present the outcomes for the multi-illuminant scenes from the LSMI dataset, again for the Galaxy, Sony, and Nikon cameras. These visualizations, paired with the quantitative error metrics, highlight the superior performance of our CST-MLP approach in multi-illuminant lighting conditions. Together, these tables and figures offer a thorough validation of our method's ability to achieve state-of-the-art colorimetric mapping.

												Ang	ular	Error	· (°)								
		~	MACs		N	likon				Ol	ympı	us			Pai	asor	nic			Sa	msur	ıg	
Method	Dim	(KB)	(M)	Mean	25%	50%	75%	90%	Mean	25%	50%	75%	90%	Mean	25%	50%	75%	90%	Mean	25%	50%	75%	90%
Oracle	1D	0.00	0.01	1.00	0.34	0.67	1.28	2.18	1.16	0.38	0.78	1.41	2.61	1.21	0.46	0.89	1.55	2.80	0.92	0.30	0.61	1.26	2.07
2-CST [1]	1D	0.07	0.01	1.65	0.64	1.16	2.19	3.69	2.10	0.89	1.62	2.81	4.08	2.11	0.76	1.61	2.85	4.72	1.69	0.78	1.27	2.28	3.46
NN [44]	1D	3.67	0.01	1.38	0.50	0.93	1.75	2.98	1.67	0.55	1.15	2.13	3.65	1.53	0.56	1.12	1.95	3.42	1.31	0.51	0.94	1.73	2.76
CST-MLP	1D	1.41	0.01	1.29	0.52	0.93	1.57	2.68	1.47	0.53	1.05	1.84	2.99	1.45	0.60	1.11	1.86	3.10	1.13	0.48	0.81	1.41	2.33
NN [44]	2D	4.04	0.01	1.41	0.49	0.96	1.84	3.08	1.64	0.54	1.17	2.12	3.50	1.52	0.56	1.11	1.97	3.46	1.37	0.49	1.01	1.83	3.02
CST-MLP	2D	1.54	0.01	1.28	0.51	0.90	1.59	2.70	1.46	0.54	1.06	1.81	2.95	1.44	0.59	1.10	1.86	3.03	1.15	0.49	0.82	1.44	2.40
													ΔE	2000									
Oracle	1D	0.00	0.01	2.29	1.21	1.94	2.88	3.99	2.60	1.41	2.21	3.08	4.74	2.67	1.41	2.26	3.58	4.61	2.08	1.20	1.79	2.54	3.57
2-CST [1]	1D	0.07	0.01	2.88	1.67	2.42	3.58	5.14	3.50	2.20	3.08	4.26	5.62	3.38	2.03	3.03	4.34	5.67	2.83	1.87	2.55	3.37	4.80
NN [44]	1D	3.67	0.01	2.57	1.45	2.19	3.21	4.64	3.07	1.79	2.66	3.83	5.46	2.91	1.58	2.46	3.89	4.98	2.42	1.49	2.12	2.95	4.06
CST-ML	1D	1.41	0.01	2.47	1.39	2.11	3.15	4.24	2.89	1.70	2.50	3.44	5.03	2.80	1.56	2.40	3.63	4.87	2.22	1.38	1.93	2.62	3.77
NN [44]	2D	4.04	0.01	2.62	1.44	2.23	3.28	4.76	3.06	1.70	2.53	3.70	5.60	2.91	1.62	2.47	3.84	4.89	2.47	1.46	2.16	3.04	4.31
CST-MLP	2D	1.54	0.01	2.46	1.40	2.10	3.06	4.28	2.87	1.65	2.44	3.43	5.08	2.80	1.60	2.42	3.64	4.82	2.23	1.41	1.95	2.66	3.71

Table S9. Quantitative evaluation on the NUS dataset. We compare the 2-CST [1] and NN [44] methods against our proposed CST-MLP using angular error and ΔE_{2000} . We find that the difference between 1D and 2D CST-MLPs is small, likely because the dataset's light sources do not strongly deviate from the Planckian Locus. Methods using our proposed 2D chromaticity input are highlighted in blue.

S4. NUS Dataset

We additionally compare on Nikon D5200 (Nikon), Olympus E-PL6 (Olympus), Panasonic Lumix DMC-GX1 (Lumix), and Samsung NX2000 (Samsung) cameras from the NUS [10] dataset. For this dataset, we again do not have access to the cameras' spectral sensitivities, so we are unable to compare with CCCNN [38] or EXPINV [33]. We report quantitative results for two cameras in Table S9. Similarly to our lightbox dataset, the 2D CST-MLP outperforms the 2-CST baseline but performs equally well as the 1D CCT CST-MLP. We believe this is caused by the illumination distribution of the NUS dataset, which is dominated by illuminants that can be effectively modeled using CCT.

S5. CCT-Based Interpolation Methods for Traditional Planckian Illuminants

The interpolation-based colorimetric mapping approaches in classical camera processing rely on accurate estimation of the scene illuminant's correlated color temperature (CCT), specifically designed for traditional light sources that approximate the Planckian locus. We outline here the computational procedures for both two-point and three-point interpolation methods, which convert observed neutral gray responses (white points) in camera RGB space to CIE xy chromaticity coordinates. While these approaches are effective for illuminants that are near the Planckian locus, they become fundamentally problematic for modern light sources that deviate significantly from the Planckian locus.

These estimation procedures address a circularity inherent in traditional camera color processing: computing the optimal color space transform requires knowledge of the illuminant's CCT, yet determining this CCT necessitates a preliminary mapping from camera space to CIE-xy coordinates before the final CST is established. However, this circular dependency assumes that all illuminants can be meaningfully characterized by a single CCT value—an assumption that breaks down for non-Planckian sources where CCT becomes ambiguous or undefined.

S5.1. Unified CCT Estimation Algorithm

Both methods utilize factory-calibrated transforms and employ an iterative refinement strategy based on Adobe's DNG processing workflow. These approaches were designed under the assumption that scene illuminants follow the blackbody radiator curve. The key difference lies in the interpolation strategy: Two-point methods use fixed calibration points at 2500 K and 6500 K [1], and Karaimer and Brown's three-point extension [27] adds a 5000 K calibration point with nearest-neighbor pair selection. The former interpolates across the full 4000 K span between calibration points. leading to maximum errors around 5000 K where interpolated transforms deviate most from optimal values. The latter reduces maximum interpolation distance to 2500 K through adaptive pair selection, improving accuracy in the problematic mid-range temperatures. Adobe subsequently adopted the three-point approach in their DNG SDK standard, recognizing its practical benefits for traditional illuminant processing. The algorithm is presented in Algorithm 1.

S5.2. Limitations

Despite the improvements, traditional 1D interpolation approaches have conceptual limitations when confronted with

modern lighting. These fundamental constraints arise from their reliance on CCT-based characterization. For LED illuminants with chromaticity coordinates significantly displaced from the Planckian locus, CCT calculations become mathematically ill-defined. Multiple CCT values may correspond to the same chromaticity point, or no meaningful CCT may exist. Readers are referred to Ohno [43] for more details.

The prevalence of LEDs and non-Planckian illuminants in modern lighting demands a shift from interpolation-based approaches to methods capable of handling the full multidimensional complexity of modern illuminants. This motivation drives our proposed neural network architecture, which abandons CCT-based characterization in favor of learning in chromaticity space for more accurate colorimetric mapping under arbitrary illumination conditions.

S6. Implementation Details

We include additional details for our implementation of the Oracle method with a least-squares solver, and CST-MLP with TinyCUDA Neural Networks (tinycadann) [39, 40].

Oracle. Our Oracle baseline uses the L-BFGS-B least-squares solver [55]. The solver is optimized to learn a 3×3 transformation by minimizing a cosine loss. We consider this solver our "Oracle", as it achieves best-case results for a 3×3 mapping.

TinyCUDA Neural Networks. TinyCUDA Neural Networks (tinycudann) is a lightweight framework designed for training highly efficient neural networks [39, 40]. We leverage this framework to train our CST-MLP, enabling fast, memory-efficient optimization while maintaining high performance on color correction tasks.

References

- [1] Adobe Inc. Adobe Digital Negative (DNG) Specification. https://helpx.adobe.com/camera-raw/digital-negative.html, 2004. Accessed: 2025-11-01. 2, 3, 4, 5, 6, 7, 8, 15, 16, 17, 18, 19, 20
- [2] Adobe Inc. Adobe Lightroom. https://lightroom.adobe.com/, 2007. Accessed: 2025-11-01. 2
- [3] Mahmoud Afifi, Luxi Zhao, Abhijith Punnappurath, Mohamed A. Abdelsalam, Ran Zhang, and Michael S. Brown. Time-aware auto white balance in mobile photography. In *ICCV*, 2025. 3
- [4] Jonathan T. Barron. Convolutional Color Constancy. In ICCV, 2015. 3
- [5] Peter R. Boyce. Human Factors in Lighting. CRC Press, 2014. 2
- [6] G. Buchsbaum. A spatial processor model for object colour perception. *Journal of the Franklin Institute*, 1980. 3

```
      Algorithm 1 Unified CCT Estimation: Two-Point and Three-Point Interpolation

      Require: Observed neutral gray in raw-RGB: n_{RGB}
```

mode:

mode

 \in

 $\begin{cases} TwoPoint, ThreePoint \} \\ \textbf{Require:} & \text{Pre-calibrated} & \text{CSTs:} & \mathbf{T}_{2500K}, & \mathbf{T}_{6500K}, \\ & [\mathbf{T}_{5000K}] & \rhd & \text{Third CST For three-point only} \end{cases}$

Require: CCT look-up-function: $CCT(x,y) \rightarrow \text{correlated color temperature}$

Ensure: Estimated CCT of scene illuminant

Require: Interpolation

```
1: x_{last} \leftarrow 0.34, y_{last} \leftarrow 0.35 \triangleright Initial coordinates
2: maxIter \leftarrow 30, tolerance \leftarrow 10^{-7}
```

3: $threshold \leftarrow 5000K$ > Pair selection threshold For three-point

```
4: for iter = 1 to maxIter do
5: CCT_{current} \leftarrow CCT(x_{last}, y_{last})
```

6: **if** mode = TwoPoint **then** \triangleright Traditional two-point interpolation

7:
$$g \leftarrow \frac{CCT_{current}^{-1} - 6500^{-1}}{2500^{-1} - 6500^{-1}}$$
8: $\mathbf{T}_{interpolated} \leftarrow g \cdot \mathbf{T}_{2500K} + (1-g) \cdot \mathbf{T}_{6500K}$
9: **else** \triangleright Three-point nearest-neighbor interpolation

10: **if** $CCT_{current} < threshold$ **then** \triangleright Use warm-neutral pair

11:
$$g \leftarrow \frac{CCT_{current}^{-1} - 5000^{-1}}{2500^{-1} - 5000^{-1}}$$
12: $\mathbf{T}_{interpolated} \leftarrow g \cdot \mathbf{T}_{2500K} + (1-g) \cdot \mathbf{T}_{g}$

 \mathbf{T}_{5000K} 13: **else** \triangleright Use neutral-cool pair

14:
$$g \leftarrow \frac{CCT_{current}^{-1} - 6500^{-1}}{5000^{-1} - 6500^{-1}}$$
15: $\mathbf{T}_{interpolated} \leftarrow g \cdot \mathbf{T}_{5000K} + (1 - g)$

 \mathbf{T}_{6500K}

16: end if

17: **end if**

18:
$$\mathbf{XYZ} \leftarrow \mathbf{T}_{interpolated} \cdot \mathbf{n}_{RGB}$$
 > Apply interpolated CST

19: $(x_{new}, y_{new}) \leftarrow \text{Convert } \mathbf{XYZ} \text{ to chromaticity coordinates}$

20: **if**
$$|x_{new} - x_{last}| + |y_{new} - y_{last}| < tolerance$$
 then 21: **break** \triangleright Convergence achieved

22: end if

23:
$$x_{last} \leftarrow x_{new}, y_{last} \leftarrow y_{new}$$

24: end for

25: **if** iter = maxIter **then** \triangleright Fallback averaging If no convergence

26:
$$x_{last} \leftarrow (x_{last} + x_{new})/2$$

27: $y_{last} \leftarrow (y_{last} + y_{new})/2$
28: **end if**

return $CCT(x_{last}, y_{last})$

[7] Marco Buzzelli. Visualizing Perceptual Differences in White Color Constancy. *Journal of Imaging Science and Technol*ogy, 67(5):1–6, 2023. 2

- [8] Calibrite LLC. ColorChecker Classic. https://calibrite.com/us/product/colorchecker-classic/, 1976. Accessed: 2025-11-01. 3, 4
- [9] Chen-Wei Chang, Cheng-De Fan, Chia-Che Chang, Yi-Chen Lo, Yu-Chee Tseng, Jiun-Long Huang, and Yu-Lun Liu. GCC: Generative Color Constancy via Diffusing a Color Checker. In CVPR, 2025. 2
- [10] Dongliang Cheng, Dilip K. Prasad, and Michael S. Brown. Illuminant estimation for color constancy: why spatial-domain methods work and the role of the color distribution. *Journal of the Optical Society of America A*, 31(5):1049–1058, 2014. 1, 8
- [11] Dongliang Cheng, Brian Price, Scott Cohen, and Michael S. Brown. Beyond White: Ground Truth Colors for Color Constancy Correction. In *ICCV*, 2015. 3
- [12] Vien Cheung, Stephen Westland, David Connah, and Caterina Ripamonti. A Comparative Study of the Characterisation of Colour Cameras by Means of Neural Networks and Polynomial Transforms. *Coloration Technology*, 120(1): 19–25, 2004. 3
- [13] Yu-Cheng Chiu, Guan-Rong Chen, Zihao Chen, and Yan-Tsung Peng. ABC-Former: Auxiliary Bimodal Cross-domain Transformer with Interactive Channel Attention for White Balance. In CVPR, 2025.
- [14] Finlayson Graham D., Steven D. Hordley, and Paul M. Hubel. Color by correlation: A simple, unifying framework for color constancy. *IEEE TPAMI*, 2001. 3
- [15] Commission Internationale de l'Éclairage (CIE). Commission Internationale de l'Éclairage Proceedings. Cambridge University Press, Cambridge, England, 1931. 1
- [16] Mauricio Delbracio, Damien Kelly, Michael S. Brown, and Peyman Milanfar. Mobile computational photography: A tour. Annual Review of Vision Science, 7:571–604, 2021. 1
- [17] S. Ferguson, Thomas. A bayesian analysis of some nonparametric problems. *The Annals of Statistics*, 1(2), 1973. 5
- [18] Graham D. Finlayson. Corrected-moment illuminant estimation. In ICCV, 2013. 3
- [19] Graham D. Finlayson, Michal Mackiewicz, and Anya Hurlbert. Color Correction Using Root-Polynomial Regression. IEEE Transactions on Image Processing, 24(5):1460–1470, 2015. 2, 3, 1
- [20] David A. Forsyth. A novel algorithm for color constancy. *International Journal of Computer Vision*, 5:5–36, 1990. 3
- [21] Arjan Gijsenij, Theo Gevers, and Joost van de Weijer. Improving color constancy by photometric edge weighting. IEEE TPAMI, 2012. 3
- [22] GTI Graphic Technology Inc. GTI ColorMatcher Series. https://www.gtilite.com/products/color-matching - systems / gti - colormatcher - series/, 2004. Accessed: 2025-11-01. 3
- [23] Daniel Hernandez-Juarez, Sarah Parisot, Benjamin Busam, Ales Leonardis, Gregory Slabaugh, and Steven McDonagh. A multi-hypothesis approach to color constancy. In CVPR, 2020. 2
- [24] Guowei Hong, Ming Ronnier Luo, and Peter A. Rhodes. A study of digital camera colorimetric characterization based on polynomial modeling. *Color Research & Application*, 2001. 1, 2

- [25] Image Engineering GmbH & Co. KG. cam-SPECS. https://www.image-engineering. de/products/equipment/measurementdevices/588-camspecs-express, 2025. Accessed: 2025-11-01. 4
- [26] Hakki C. Karaimer and Michael S. Brown. A Software Platform for Manipulating the Camera Imaging Pipeline. In ECCV, 2016. 2
- [27] Hakki C. Karaimer and Michael S. Brown. Improving Color Reproduction Accuracy on Cameras. In CVPR, 2018. 2, 3, 4, 5, 6, 7, 8, 12, 13, 14
- [28] Vinod K. Khanna. Fundamentals of Solid-State Lighting. CRC Press, 2014. 2
- [29] Dongyoung Kim, Jinwoo Kim, Seonghyeon Nam, Dongwoo Lee, Yeonkyung Lee, Nahyup Kang, Hyong-Euk Lee, ByungIn Yoo, Jae-Joon Han, and Seon Joo Kim. Large Scale Multi-Illuminant (LSMI) Dataset for Developing White Balance Algorithm Under Mixed Illumination. In *ICCV*, 2021. 4, 7, 8, 1, 5, 15, 16, 17, 19, 20
- [30] Dongyoung Kim, Jinwoo Kim, Junsang Yu, and Seon Joo Kim. Attentive Illumination Decomposition Model for Multi-Illuminant White Balancing. In CVPR, 2024.
- [31] Dongyoung Kim, Mahmoud Afifi, Dongyun Kim, Michael S. Brown, and Seon Joo Kim. Ccmnet: Leveraging calibrated color correction matrices for cross-camera color constancy. In *ICCV*, 2025. 3
- [32] Diederik P. Kingma and Jimmy Ba. Adam: A Method for Stochastic Optimization. In *ICLR*, 2015. 5
- [33] Abdullah Kucuk, Graham D. Finlayson, Rafal Mantiuk, and Maliha Ashraf. An Exposure Invariant Neural Network for Colour Correction. In *Color and Imaging Conference*, 2022. 3, 4, 5, 6, 7, 8, 12, 13, 14
- [34] Selena Ling, Merlin Nimier-David, Alec Jacobson, and Nicholas Sharp. Stochastic preconditioning for neural field optimization. In SIGGRAPH, 2025. 5
- [35] Yi-Chen Lo, Chia-Che Chang, Hsuan-Chao Chiu, Yu-Hao Huang, Chia-Ping Chen, Yu-Lin Chang, and Kevin Jou. Clcc: Contrastive learning for color constancy. In CVPR, 2021. 3
- [36] Alexander D. Logvinenko, Brian Funt, Hamidreza Mirzaei, and Rumi Tokunaga. Rethinking Colour Constancy. PLOS One, 2015. 8, 3
- [37] Zhongyu Lou, Theo Gevers, Ninghang Hu, and Marcel P. Lucassen. Color constancy by deep learning. In BMVC, 2015. 3
- [38] Lindsay MacDonald and Katarina Mayer. Camera Colour Correction using Neural Networks. In *London Imaging Meeting*, 2021. 3, 4, 5, 6, 7, 8
- [39] Thomas Müller, Fabrice Rousselle, Jan Novák, and Alexander Keller. Realtime neural radiance caching for path tracing. In *ACM Trans. Graph.*, 2021. 9
- [40] Thomas Müller, Alex Evans, Christoph Schied, and Alexander Keller. Instant neural graphics primitives with a multiresolution hash encoding. *ACM Trans. Graph.*, 2022. 9
- [41] Albert H. Munsell. A Color Notation (12th Edition). Munsell Color Company, 1971. 5

- [42] Michael J. Murdoch. Characterization and Control of a Multi-primary LED Light Lab. Optics Express, 25(24): 29605–29616, 2017. 2
- [43] Yoshi Ohno. Practical Use and Calculation of CCT and Duv. LEUKOS, The Journal of the Illuminating Engineering Society, 10(1):47–55, 2013. 2, 9
- [44] Leif E Peterson. K-nearest neighbor. *Scholarpedia*, 4(2): 1883, 2009. 4, 6, 7, 8, 15, 16, 17, 18, 19, 20
- [45] Abhijith Punnappurath, Luxi Zhao, Hoang Le, Abdelrahman Abdelhamed, SaiKiran Kumar Tedla, and Michael S. Brown. Improved mapping between illuminations and sensors for RAW images. *Journal of the Optical Society of America A*, 42(8):1182–1190, 2025. 3, 1, 5
- [46] Alec Radford, Jong Wook Kim, Chris Hallacy, Aditya Ramesh, Gabriel Goh, Sandhini Agarwal, Girish Sastry, Amanda Askell, Pamela Mishkin, Jack Clark, Gretchen Krueger, and Ilya Sutskever. Learning Transferable Visual Models From Natural Language Supervision. In ICML, 2021. 4
- [47] Eric F. Schubert. Light-Emitting Diodes. 2023. 2
- [48] David Serrano-Lozano, Aditya Arora, Luis Herranz, Konstantinos G. Derpanis, Micheal S. Brown, and Javier Vazquex-Corral. Revisiting image fusion for multi-illuminant white-balance correction. In *ICCV*, 2025. 2, 3
- [49] Saikiran Tedla, Yunyuan Wang, Maitri Patel, and Michael S. Brown. Analyzing color imaging failure on consumer-grade cameras. *Journal of the Optical Society of America*, 2022. 8, 3
- [50] Telelumen LLC. Octa Light Player. https: //telelumen.com/wp-content/uploads/2023/ 11 / telelumen - booth - option - brochure -230217.pdf, 2004. Accessed: 2025-11-01. 3
- [51] Joost van de Weijer, Theo Gevers, and Arjan Gisenji. Edgebased color constancy. *IEEE TIP*, 2007. 3
- [52] Hao Wang, Yitong Wang, Zheng Zhou, Xing Ji, Dihong Gong, Jingchao Zhou, Zhifeng Li, and Wei Liu. Cosface: Large margin cosine loss for deep face recognition. In CVPR, 2018. 4
- [53] Günter Wyszecki and Walter S. Stiles. *Color Science (2nd Edition)*. Wiley, 2000. 1, 3
- [54] Fangneng Zhan, Yingchen Yu, Changgong Zhang, Rongliang Wu, Wenbo Hu, Shijan Lu, Feiying Ma, Xuansong Xie, and Ling Sha. GMLight: Lighting Estimation via Geometric Distribution Approximation. *IEEE TIP*, 2021. 2
- [55] Ciyou Zhu, Richard H. Byrd, Peihang Lu, and Jorge Nocedal. Algorithm 778: L-bfgs-b: Fortran subroutines for large-scale boundconstrained optimization. ACM Trans. Math. Softw., 1997. 9

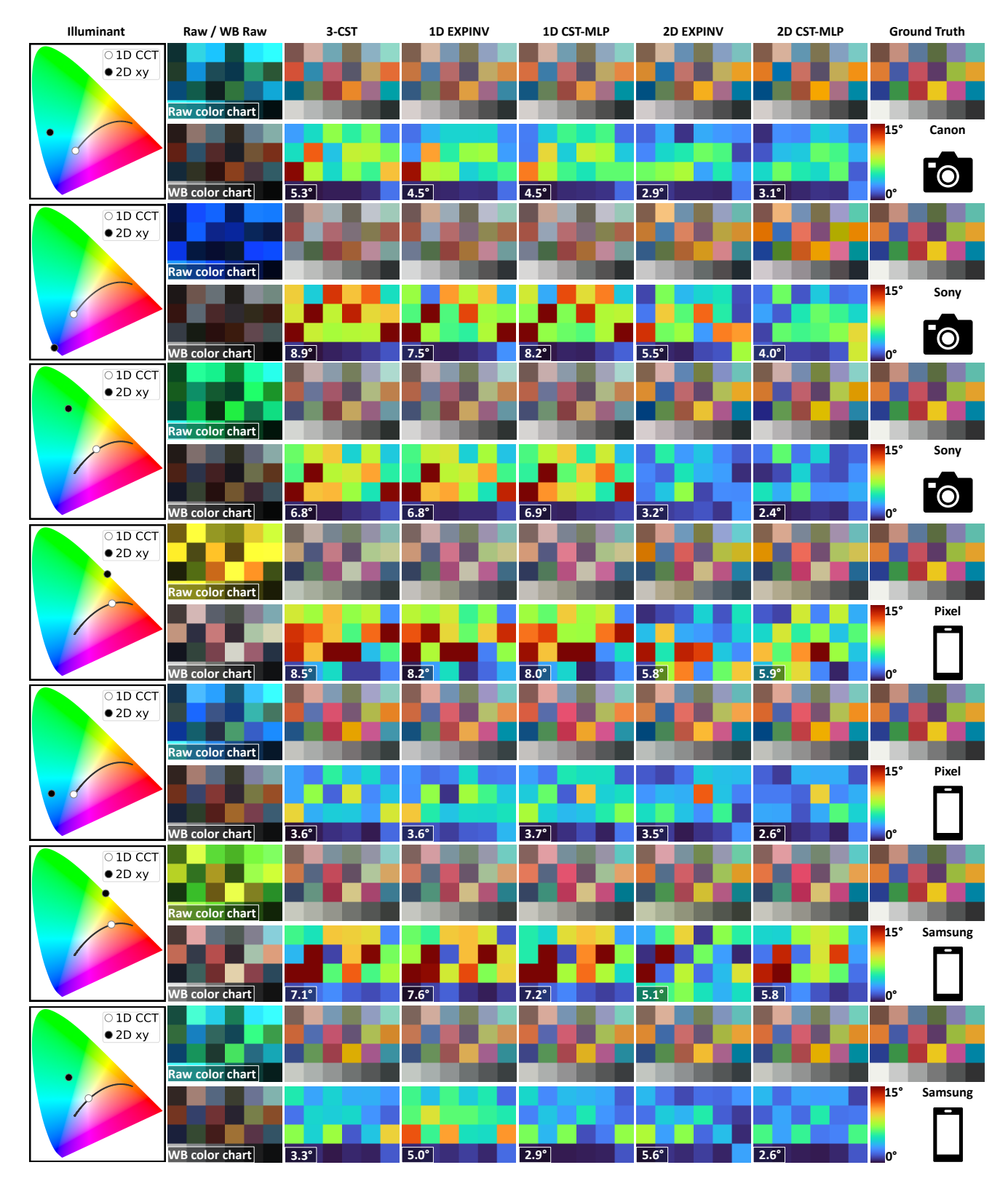


Figure S4. Colorimetric mapping results on lightbox dataset. Results for seven different non-Planckian LED illuminant and camera combinations: two examples for Sony, two for Pixel, two for Samsung, and one for Canon. Each of the seven blocks starts with the illuminant's CCT and xy chromaticity and contains two rows: the top row shows the raw-RGB color chart, and the display-referred renderings for each method; the bottom row shows the white-balanced color chart and corresponding angular error maps. Methods: 2-CST [27], 1D EXPINV [33], our 1D CST-MLP, 2D EXPINV [33], our 2D CST-MLP, and ground truth. Key findings: (1) Traditional 1D methods exhibit substantial errors for off-locus illuminants. (2) 2D chromaticity representation improves existing methods (compare 1D vs. 2D for EXPINV and CST-MLP).

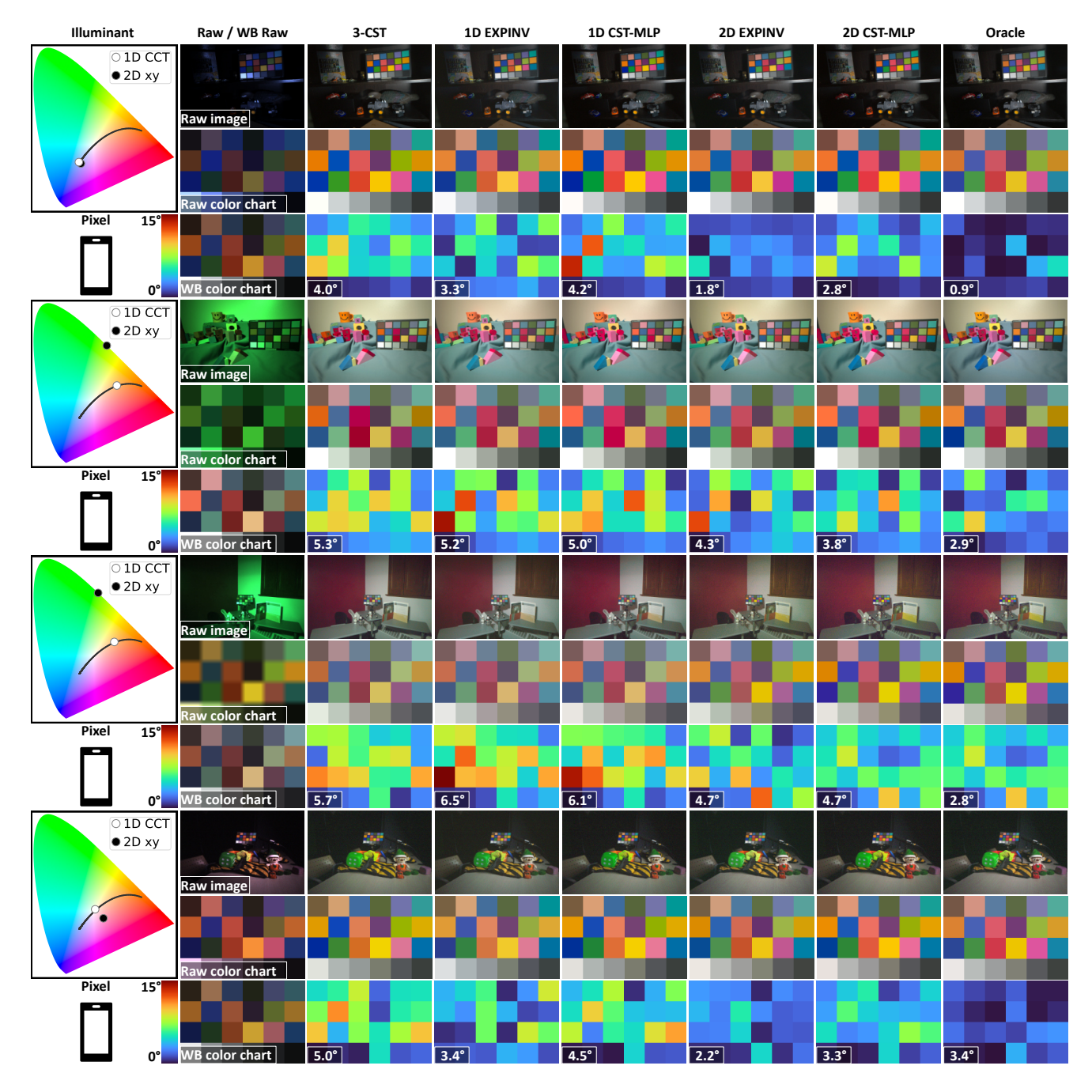


Figure S5. Colorimetric mapping results on in-the-wild captures (Pixel camera). This figure provides an expanded set of results, supplementing the two examples shown in the main paper. Results are shown for four different light sources captured using the Pixel camera. Each section corresponds to a different illuminant, starting with its CCT and xy chromaticity, and is organized into three rows: the top row shows the raw-RGB image and display-referred renderings; the middle row shows the raw-RGB color chart and display-referred renderings; the bottom row shows the white-balanced color chart and angular error maps. Methods: 3-CST [27], 1D EXPINV [33], our 1D CST-MLP, 2D EXPINV [33], our 2D CST-MLP, and Oracle. **Key findings:** (1) 2D methods outperform 1D methods under these in-the-wild lighting conditions. (2) Per-pixel methods such as EXPINV [33] can suffer from color casts.

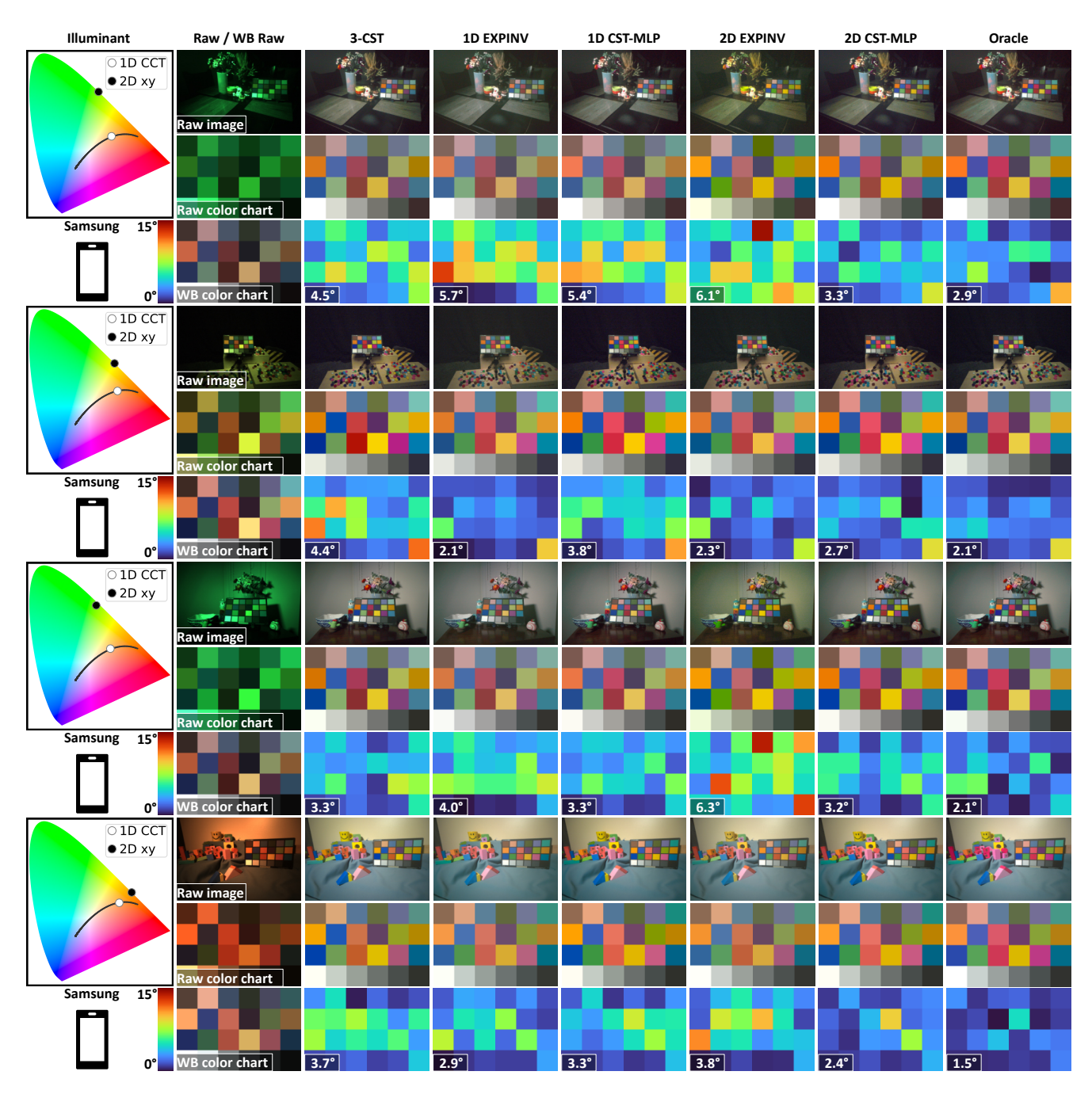


Figure S6. Colorimetric mapping results on in-the-wild captures (Samsung camera). This figure provides an expanded set of results, supplementing the two examples shown in the main paper. Results are shown for four different light sources captured using the Samsung camera. Each section corresponds to a different illuminant, starting with its CCT and xy chromaticity, and is organized into three rows: the top row shows the raw-RGB image and display-referred renderings; the middle row shows the raw-RGB color chart and display-referred renderings; the bottom row shows the white-balanced color chart and angular error maps. Methods: 3-CST [27], 1D EXPINV [33], our 1D CST-MLP, 2D EXPINV [33], our 2D CST-MLP, and Oracle. **Key findings:** (1) 2D methods outperform 1D methods under these in-the-wild lighting conditions. (2) Per-pixel methods such as EXPINV [33] can suffer from color casts.

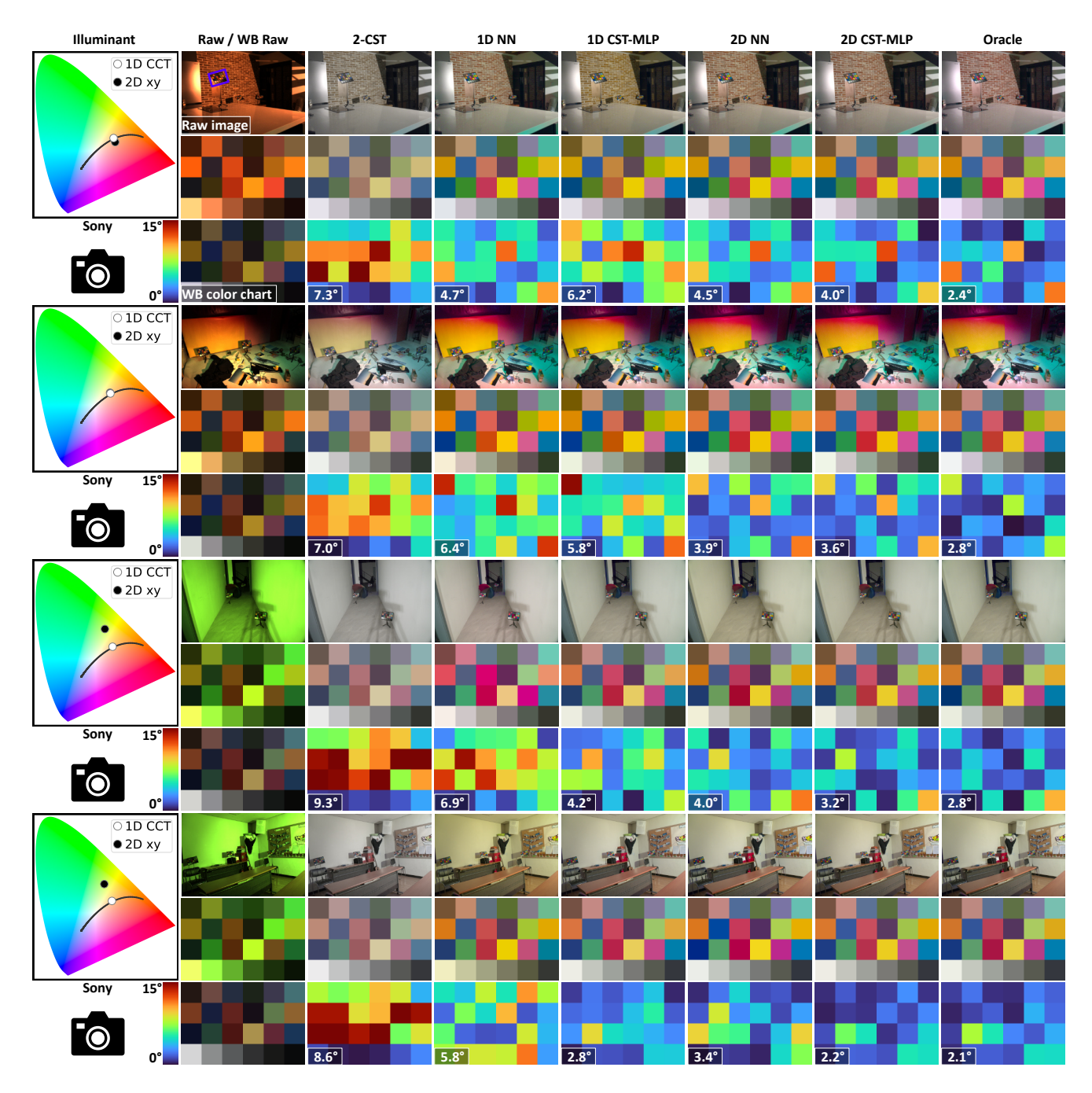


Figure S7. Colorimetric mapping results on single-illuminant data from LSMI [29] (Sony camera). While the main paper focused on multi-illuminant scenes due to space constraints, this figure presents a detailed evaluation on single-illuminant data. Each section corresponds to a different illuminant, starting with its CCT and xy chromaticity, and is organized into three rows: The top row displays the full raw-RGB image alongside the display-referred renderings; the middle row shows the raw-RGB color chart and its rendered versions; and the bottom row presents the white-balanced color chart with angular error maps. Methods (from left to right): 2-CST [1], 1D NN [44], our 1D CST-MLP, 2D NN [44], our 2D CST-MLP, and Oracle. Analysis: The visual evidence across these examples reinforces our quantitative results, consistently demonstrating the superior color reproduction of our 2D CST-MLP.

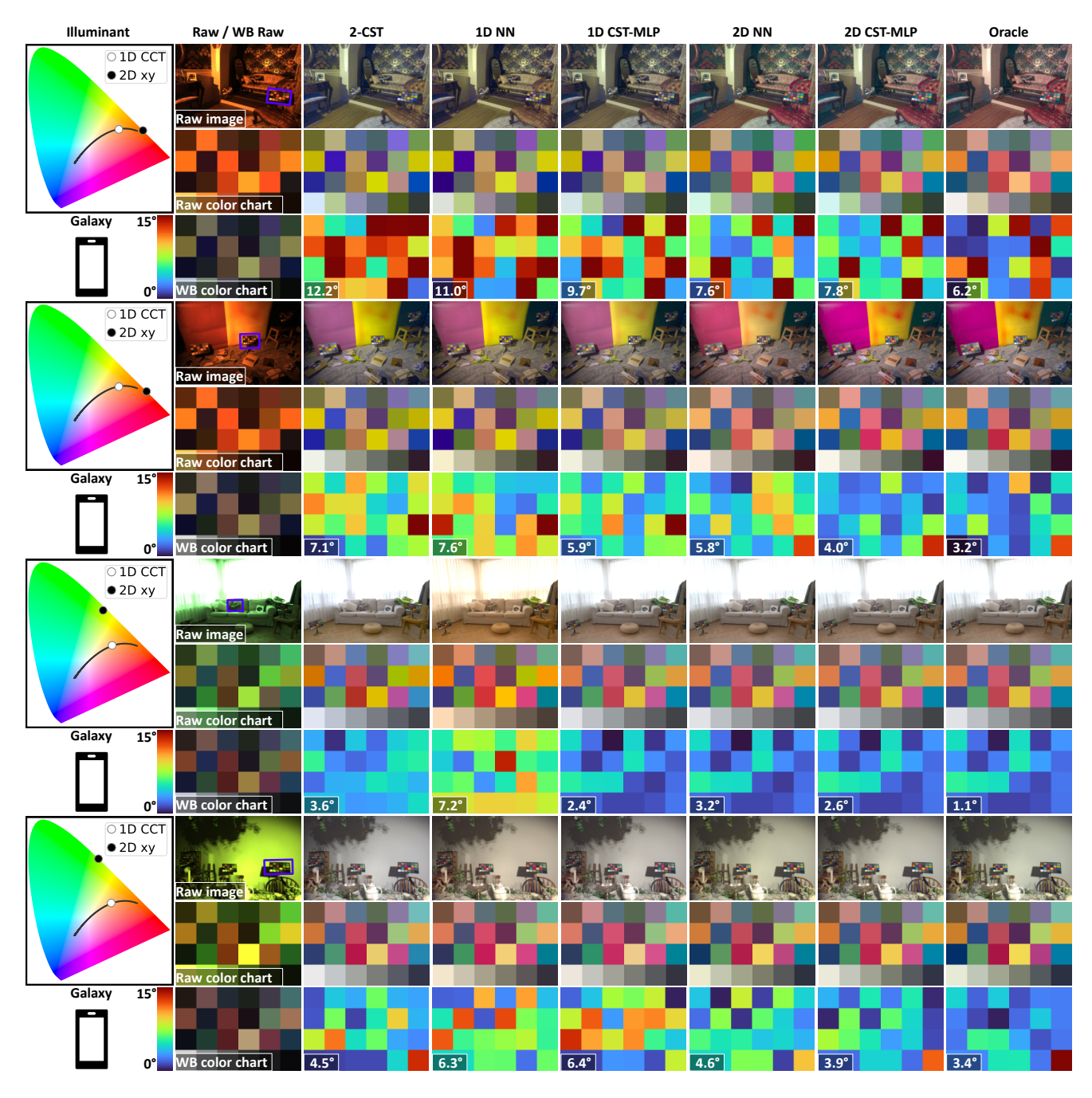


Figure S8. Colorimetric mapping results on single-illuminant data from LSMI [29] (Galaxy camera). To complement the multi-illuminant analysis in the main paper, we now show results on single-illuminant scenes, which were omitted for brevity. Each section corresponds to a different illuminant, starting with its CCT and xy chromaticity, and is organized into three rows. The first row provides full scene context with final renderings. The subsequent rows offer detailed views, with the second focusing on the raw color chart and its renderings, and the third displaying the white-balanced chart and corresponding angular error maps. **Methods (from left to right):** 2-CST [1], 1D NN [44], our 1D CST-MLP, 2D NN [44], our 2D CST-MLP, and Oracle. **Analysis:** These results visually affirm the limitations of 1D methods even in less complex scenes, where our 2D approach produces noticeably more accurate color.

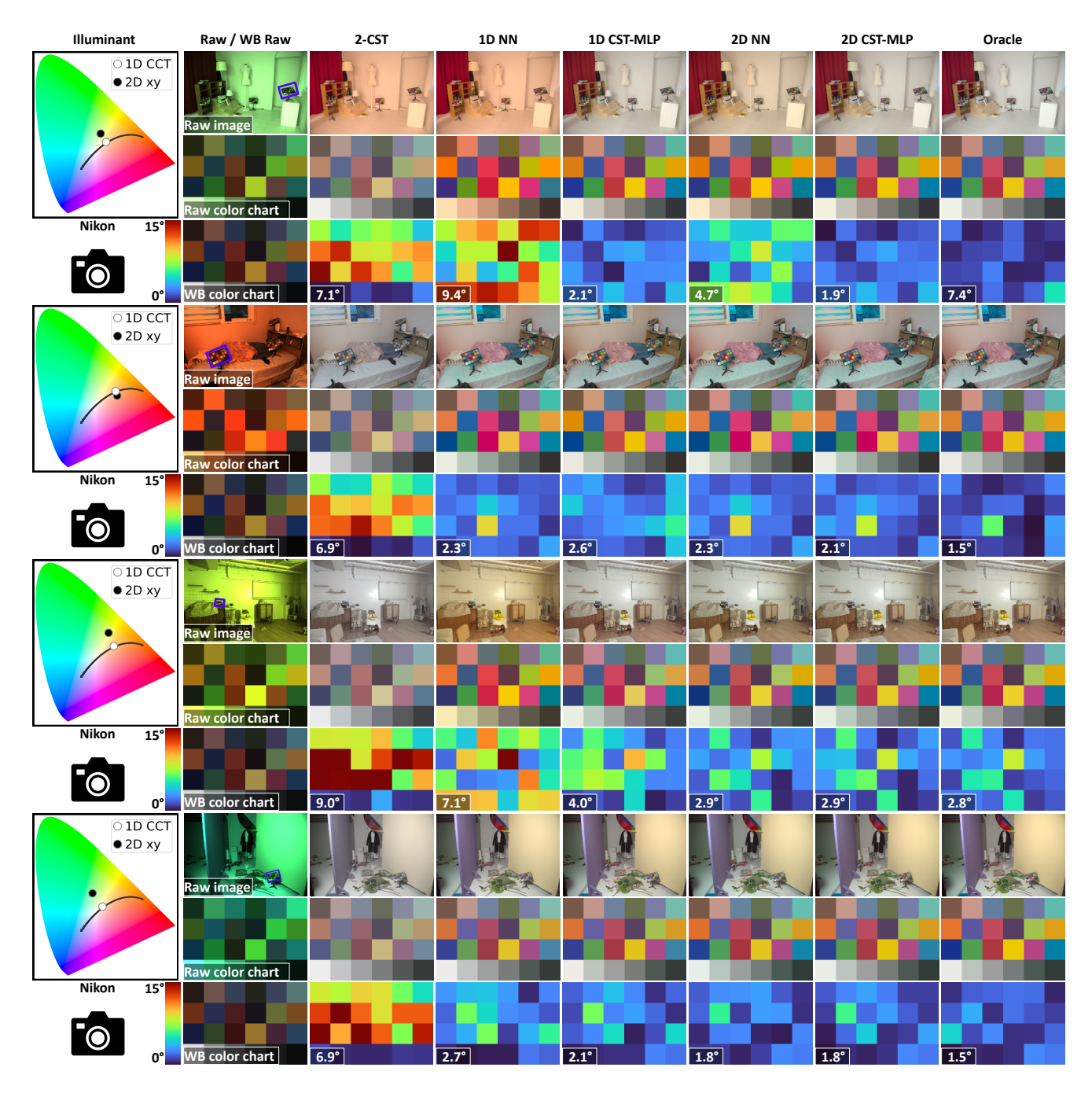


Figure S9. Colorimetric mapping results on single-illuminant data from LSMI [29] (Nikon camera). The main paper prioritized an analysis of challenging multi-illuminant scenes. Here, we provide the corresponding single-illuminant results to offer a complete performance picture. Each section corresponds to a different illuminant, starting with its CCT and xy chromaticity, and is organized into three rows. The rows display: (1) the full raw scene and final outputs, (2) the raw color chart with its display-referred renderings, and (3) the white-balanced chart paired with visualizations of angular error. **Methods (from left to right):** 2-CST [1], 1D NN [44], our 1D CST-MLP, 2D NN [44], our 2D CST-MLP, and Oracle. **Analysis:** Across these diverse lighting conditions, the error maps and rendered charts visually corroborate our central claim: our 2D CST-MLP consistently provides more accurate color corrections than its 1D counterparts.

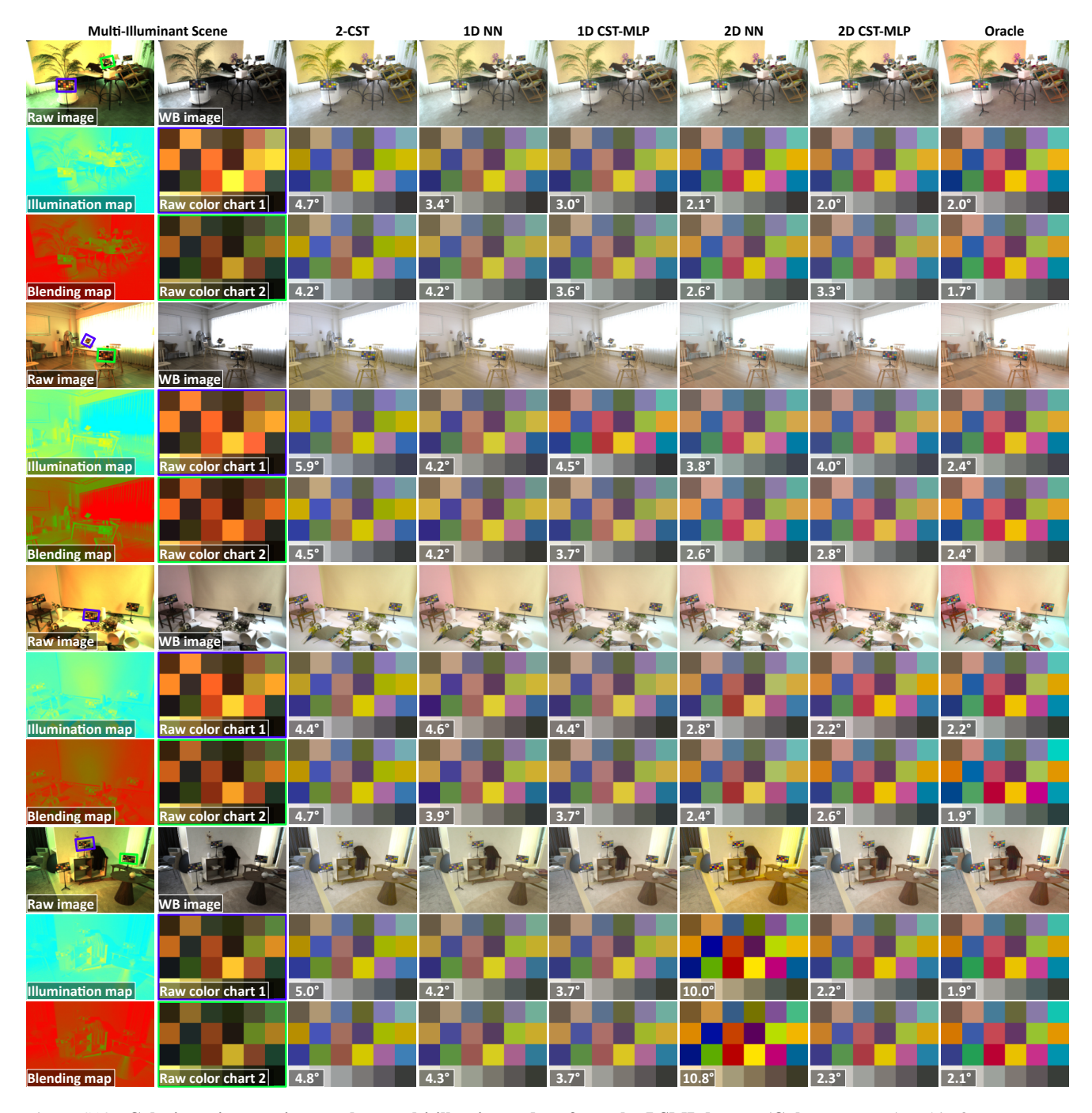


Figure S10. Colorimetric mapping results on ulti-illuminant data from the LSMI dataset (Galaxy camera). This figure presents an expanded qualitative evaluation, showcasing four spatially-varying multi-illuminant scenes to supplement the two shown in the main paper. Layout for each scene: The top row displays the input raw-RGB image, the white-balanced image, and the final display-referred renderings. The middle row visualizes the contrast-stretched illumination map, the first raw-RGB color chart, and its corrected renderings. The bottom row shows the per-pixel blending map, the second raw-RGB color chart, and its corresponding renderings. Methods (from left to right): 2-CST [1], 1D NN [44], our 1D CST-MLP, 2D NN [44], our 2D CST-MLP, and Oracle. Mean angular errors are provided at the bottom left of each rendered chart. Observations: These additional results further validate our method's effective extension to complex scenes and confirm the consistent performance advantage of 2D chromaticity-based approaches over 1D methods.

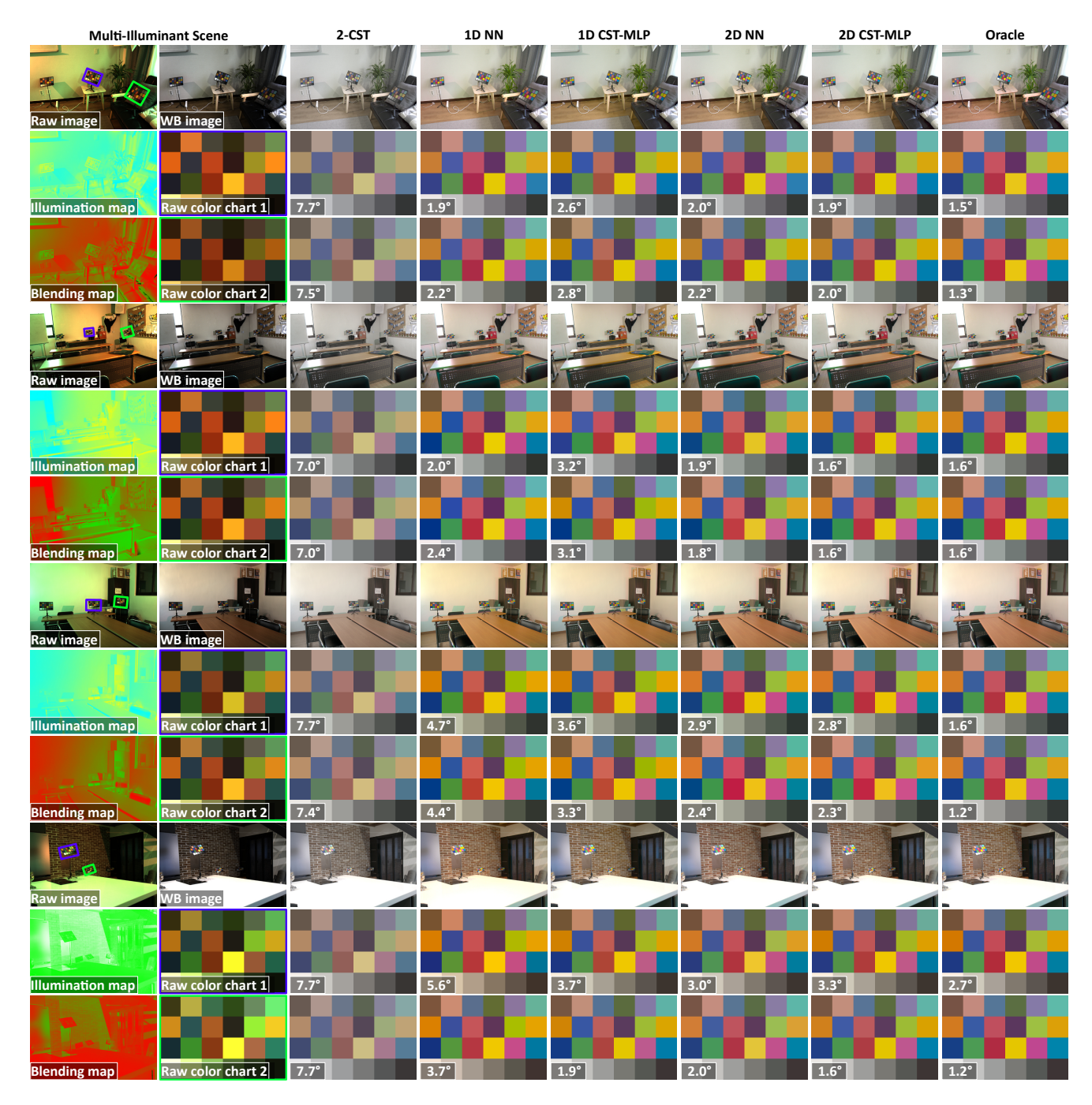


Figure S11. Colorimetric mapping results on ulti-illuminant data from the LSMI dataset (Sony camera). We provide expanded colorimetric mapping results for the Sony camera, showcasing four multi-illuminant scenes from the LSMI dataset [29]. These build upon the two examples presented in the main paper. Layout for each scene: Each of the four scenes is detailed across three rows. Row 1: Original raw-RGB input, the white-balanced version, and final rendered outputs. Row 2: The illumination map, the first raw-RGB color chart, and its rendered results. Row 3: The blending map, the second raw-RGB color chart, and its rendered results. Methods (from left to right): 2-CST [1], 1D NN [44], our 1D CST-MLP, 2D NN [44], our 2D CST-MLP, and Oracle. Angular errors are displayed on each rendered color chart. Observations: These comprehensive visualizations reinforce the robustness of our 2D CST-MLP in handling spatially-varying illumination and its superior accuracy compared to 1D techniques across different camera sensors.

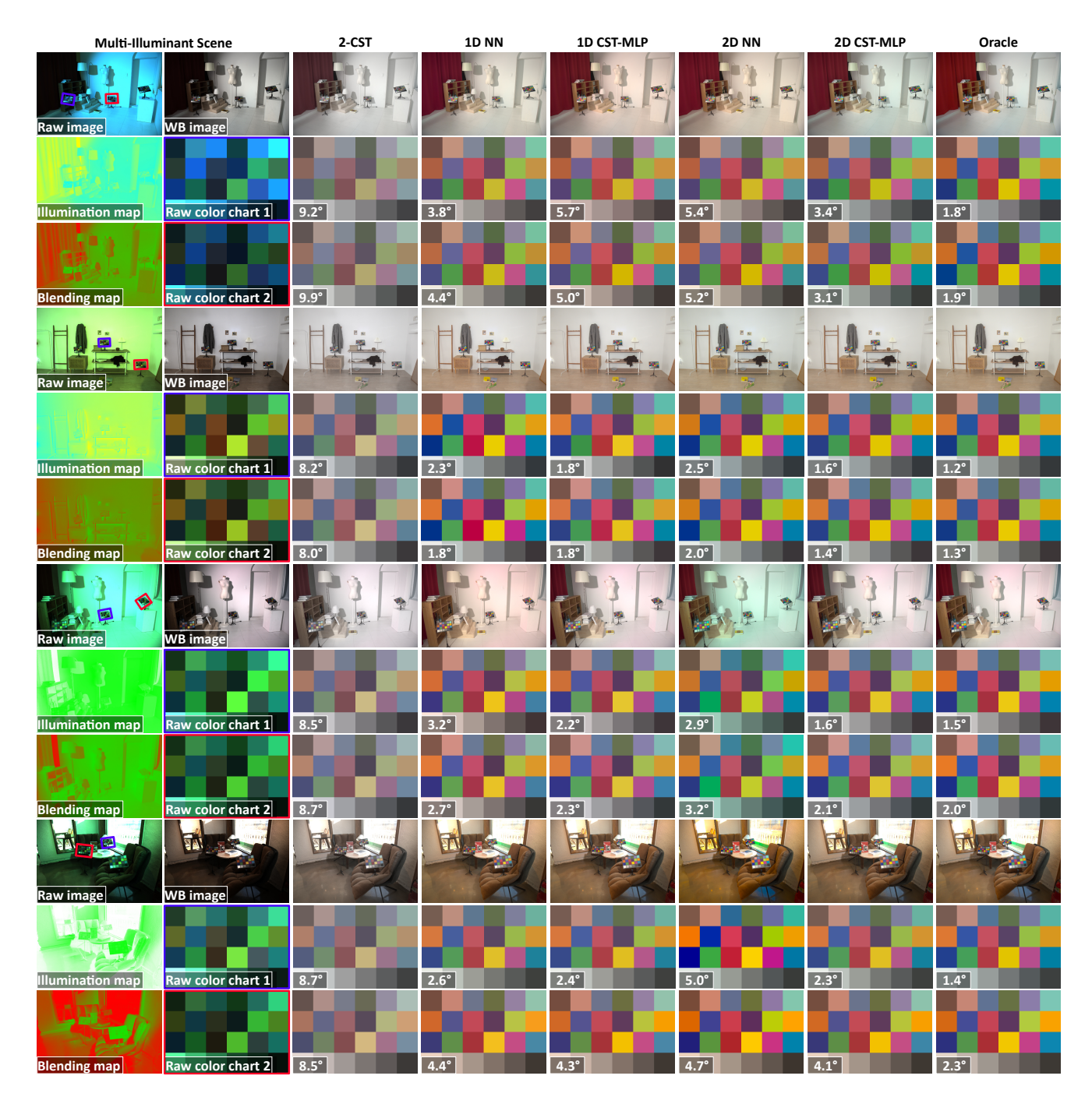


Figure S12. Colorimetric mapping results on ulti-illuminant data from the LSMI dataset (Nikon camera). This figure offers further qualitative validation with four challenging multi-illuminant scenes from the LSMI dataset [29], providing a more comprehensive view than the two scenes in the main paper. Layout for each scene: For each of the four scenes, the visualization is organized as follows: (top row) the input raw image, the result after white balancing, and final corrected outputs from all methods; (middle row) the illumination map and its corrected renderings of the first color chart; (bottom row) the blending map and its corresponding renderings of the second color chart. Methods (from left to right): 2-CST [1], 1D NN [44], our 1D CST-MLP, 2D NN [44], our 2D CST-MLP, and Oracle. Quantitative angular errors are noted on each rendered chart. Observations: As with other cameras, these extensive results for the Nikon sensor underscore the capability of our 2D CST-MLP to manage complex, mixed-lighting conditions, outperforming methods that rely on a single-dimensional illuminant representation.